

Numerical study of multiscale compaction-initiated detonation

J. R. Gambino¹ · D. W. Schwendeman²  · A. K. Kapila²

Received: 28 July 2017 / Revised: 29 November 2017 / Accepted: 10 January 2018 / Published online: 7 February 2018
© Springer-Verlag GmbH Germany, part of Springer Nature 2018

Abstract A multiscale model of heterogeneous condensed-phase explosives is examined computationally to determine the course of transient events following the application of a piston-driven stimulus. The model is a modified version of that introduced by Gonthier (Combust Sci Technol 175(9):1679–1709, 2003. doi:10.1080/00102200302373) in which the explosive is treated as a porous, compacting medium at the macro-scale and a collection of closely packed spherical grains capable of undergoing reaction and diffusive heat transfer at the meso-scale. A separate continuum description is ascribed to each scale, and the two scales are coupled together in an energetically consistent manner. Following piston-induced compaction, localized energy deposition at the sites of intergranular contact creates hot spots where reaction begins preferentially. Reaction progress at the macro-scale is determined by the spatial average of that at the grain scale. A parametric study shows that combustion at the macro-scale produces an unsteady detonation with a cyclical character, in which the lead shock loses strength and is overtaken by a stronger secondary shock generated in the partially reacted material behind it. The secondary shock in turn becomes the new lead shock and the process repeats itself.

Keywords Reactive flow · Detonation · Multiphase flow · Multiscale modeling · Godunov methods

1 Introduction

It has long been understood that combustion of a heterogeneous explosive is a multiscale phenomenon. Chemical reactions occur and release energy at the molecular level, while the thermal and mechanical consequences resulting therefrom are manifest at the much larger macro-scale (or bulk scale) of observation and measurement. In a homogeneous material, the response at the macro-scale is reasonably well-characterized by continuum descriptions designed to capture the averaged behavior. Such descriptions are insufficient, however, when the material is heterogeneous, as they fail to account adequately for the effect of grain-scale (or meso-scale) microstructure on the features observed at the macro-scale. For example, when a heterogeneous explosive is subjected to shock loading, the stress field generated behind the shock is nonuniform due to localized energy deposition and rapid deformation caused by a variety of mechanisms in the vicinity of the grain-to-grain contacts. As a result, the temperature field is nonuniform as well, with localized hot spots resulting in preferential initiation of chemical activity at discrete sites before the reaction spreads to the bulk. Even if the grain-scale behavior were well-understood, and mathematical models incorporating this knowledge were available, accurate numerical computations would require fine resolution of sub-grain scales, a task that is not routinely feasible yet.

A practical approach of accounting for the microstructure has been to model the explosive as a single-phase or multiphase mixture at the macro-scale and introduce the sub-scale information into the model in the form of constitutive laws,

Communicated by D. Zeidan and H. D. Ng.

✉ D. W. Schwendeman
schwede@rpi.edu

¹ Lawrence Livermore National Laboratory, Livermore, CA 94550, USA

² Department of Mathematical Sciences, Rensselaer Polytechnic Institute, Troy, NY 12180, USA

especially reaction kinetics. A range of such models exists, from fully homogenized Euler-equation models proposed by Tarver et al. [2–4] in which the explosive is a single-phase homogeneous mixture of reactant and product, to more complex two-phase models of the Baer–Nunziato type [5]; also see [6–15]. Hybrid models incorporating features of both the Euler-equation and the Baer–Nunziato models have also been suggested [16]. With close experimental calibration and suitable choices of constitutive parameters, these models are able to predict a limited range of experimental observations. They are less successful in providing a description of phenomena such as initiation caused by weak stimuli in accident scenarios, and the effect of aging-induced microstructural changes on explosive sensitivity and performance. A renewed interest in obtaining improved understanding of these phenomena has motivated studies aimed at more accurate descriptions of grain-scale processes and their coupling with events at the macro-scale.

A thorough review of meso-scale modeling of heterogeneous explosives is provided by Baer [17]; also see the references contained therein. It summarizes the various modeling approaches being pursued, including direct numerical simulation of microstructural response. It is clear from the review that while much progress has been achieved, a predictive model in which the diverse scales are coupled with sufficient fidelity and for which the relevant constitutive inputs are available remains elusive. While the pursuit of such a holistic model is important, it is also useful to examine simpler models of coupling of scales, which focus on certain dominant mechanisms at the grain scale, to determine what their capabilities are and to what extent they are able to capture observed phenomena.

Gonthier [1] introduced a model of this kind that included the evolution of bulk-scale events and also of processes at the grain scale. Material at the bulk scale was modeled as an incompressible continuum with a compaction law and was coupled to a grain-scale model that tracked the evolution of hot spots in the microstructure. The grain-scale solution, resulting from an interplay between localized energy deposition, diffusive heat transfer, and chemical reaction in the grains, was averaged to provide a chemical source for the bulk-scale description. Steady, traveling wave solutions were computed, and it was found that weak piston impacts could lead to temperatures high enough for the onset of sustained combustion.

Zhang et al. [18] simulated the generation of an ensemble of shock-induced hot spots in an otherwise homogeneous medium by introducing them as spots of reduced density. Both periodic and random arrays were considered, and conclusions were drawn about the critical density of hot spots needed for transition to detonation. In a later paper, Jackson et al. [19] focused on pore collapse as the primary grain-scale mechanism responsible for the generation of hot

spots. A detailed model of pore collapse was analyzed and employed to formulate a power deposition function that could be assigned to each hot spot in computations with a homogeneous macro-scale description. Multiple arrays in various configurations were examined to evaluate the effect of array geometry on transition to detonation. Recently Zhang and Jackson [20] have employed a similar approach to assess the influence of hot-spot size on the propensity to detonate.

In this work we return to a modified version of Gonthier's model cited above [1]. While his work had focused on steady traveling waves, our emphasis is on transient wave development following a piston impact. We take a comprehensive look at the mechanisms that are responsible for the generation and subsequent propagation of the detonation. Detailed results are presented for three representative parameter choices. It is found that none of the cases exhibits a steady traveling wave; rather, combustion proceeds in a cyclical fashion in each case. Typically, a primary lead shock induced by compaction and supported by reaction loses strength as it propagates through ambient material. Reaction in the partially reacted material behind the primary shock generates a stronger and faster secondary shock which overtakes the primary shock to become the new lead shock, and the process repeats itself. Although the precise mechanisms responsible for the creation of the secondary shock are dependent upon the prevailing parameters, it is found that the general features of the evolution are preserved from one case to the next.

The paper is organized as follows. Governing equations for the model are presented in Sect. 2. Appropriate reference scales are chosen and the model is rendered dimensionless in Sect. 3. Section 4 discusses the numerical method used to obtain solutions, and Sect. 5 verifies the convergence of the numerical procedure. Detailed results of the computations are presented and discussed in Sect. 6. Concluding remarks are made in Sect. 7.

2 Multiscale model

The starting point of our study is a modified version of the multiscale model proposed by Gonthier [1]. At the bulk scale, the granular explosive is treated as a porous reactive solid and modeled as a homogeneous continuum occupying a fraction of the available volume. Gonthier's assumption of the solid being incompressible is relaxed. At the scale of the grains, the material is again modeled as a homogeneous continuum, undergoing chemical reaction and diffusive heat transport. The two scales are coupled by energy transfer and reaction progress. Reaction progress at the bulk scale is defined as the average of the reaction progress at the grain scale. In effect, the grain-scale model can be viewed as an elaborate reaction-kinetics model for the bulk scale. We employ the model to

examine, in the reverse-impact configuration, evolution subsequent to piston impact.

2.1 Bulk-scale equations

At the bulk scale, we consider a spatially one-dimensional configuration with the porous explosive packed into a cylindrical tube of length L . A volume-fraction variable is introduced to account for the porosity. Only the flow of the solid is considered and the gas occupying the pores is neglected. Thus, at the bulk scale the model is a reduced variant of the two-phase Baer–Nunziato model for granular explosives described in [5]. The governing equations are

$$\frac{\partial}{\partial t} (\alpha\rho) + \frac{\partial}{\partial x} (\alpha\rho u) = 0, \tag{1}$$

$$\frac{\partial}{\partial t} (\alpha\rho u) + \frac{\partial}{\partial x} (\alpha\rho u^2 + \alpha p) = 0, \tag{2}$$

$$\frac{\partial}{\partial t} (\alpha\rho E) + \frac{\partial}{\partial x} (\alpha\rho u E + \alpha u p) = 0, \tag{3}$$

$$\frac{\partial \alpha}{\partial t} + u \frac{\partial \alpha}{\partial x} = \mathcal{F}, \tag{4}$$

where α is the volume fraction of the solid, ρ is the density, u is the velocity, p is the pressure, and E is the total energy, all depending on the position x and time t . Equations (1)–(3) are conservation laws for mass, momentum, and energy of the solid phase, respectively, while (4) describes the compaction of the solid phase with compaction rate

$$\mathcal{F} = \frac{\alpha(1-\alpha)}{\mu_c} (p - \beta). \tag{5}$$

Here μ_c is the (constant) compaction viscosity and β is the configuration pressure given by

$$\beta = \alpha\rho \frac{d}{d\alpha} B(\alpha), \tag{6}$$

where $B(\alpha)$ is the compaction potential.¹ Following [15] we take

$$B(\alpha) = -\frac{p_0(2-\alpha_0)^2}{\alpha_0\rho_0 \ln(1-\alpha_0)} \times \ln \left[\left(\frac{2-\alpha}{2-\alpha_0} \right) \frac{(1-\alpha)^{(1-\alpha)/(2-\alpha)}}{(1-\alpha_0)^{(1-\alpha_0)/(2-\alpha_0)}} \right], \tag{7}$$

¹ The origin and physical interpretation of the quantities appearing (5), and of the compaction potential introduced in (6), are discussed in detail in [5, 10].

where the zero subscript denotes quantities at the ambient state. The total energy in (3) is given by

$$E = e + \frac{u^2}{2} + B(\alpha),$$

where e is the internal energy. A stiffened-gas equation of state is adopted for the solid having the form

$$e = \frac{p + \gamma\pi}{(\gamma - 1)\rho} - q\lambda, \tag{8}$$

where γ is the ratio of specific heats, π is the stiffening pressure, q is the heat release due to reaction, and λ is the bulk-scale reaction-progress variable, with $\lambda = 0$ corresponding to the absence of reaction and $\lambda = 1$ to a complete conversion of the reactant. For later purposes we note that the temperature T and sound speed c of the solid at the bulk scale are given by

$$C_v T = e - \frac{\pi}{\rho} + q\lambda, \quad c^2 = \frac{\gamma(p + \pi)}{\rho}, \tag{9}$$

where C_v is the specific heat of the solid at constant volume, taken to be a constant.

Equations (1)–(4) can be viewed as equations for the four primitive variables (α, ρ, u, p) at the bulk scale, with the additional variable λ determined by a model for the reaction kinetics. This reaction model is given by the description at the grain scale which consists of rate equations for a grain-scale reaction-progress variable and a grain-scale temperature. The bulk-scale λ is then specified as an average of the reaction progress at the grain scale as described in Sects. 2.2 and 2.3.

For the reverse-impact problem the initial conditions for the bulk-scale variables are taken to be

$$\alpha = \alpha_0, \quad \rho = \rho_0, \quad u = -u_p, \quad p = p_0, \quad \lambda = 0, \quad \text{at } t = 0,$$

where α_0 , ρ_0 , and p_0 are, respectively, the ambient volume fraction, density and pressure of the solid explosive and $u_p > 0$ is the piston velocity. The ambient temperature T_0 and the sound speed c_0 are then given by the formulas

$$C_v T_0 = \frac{p_0 + \pi}{(\gamma - 1)\rho_0}, \quad c_0^2 = \frac{\gamma(p_0 + \pi)}{\rho_0},$$

in view of (8) and (9). The left boundary is considered to be the piston face where we impose the symmetry boundary conditions

$$\frac{\partial \alpha}{\partial x} = \frac{\partial \rho}{\partial x} = \frac{\partial p}{\partial x} = 0, \quad u = 0, \quad \text{at } x = 0.$$

The right-hand side of the domain, $x = L$, is taken to be sufficiently far from the piston face so that the disturbances

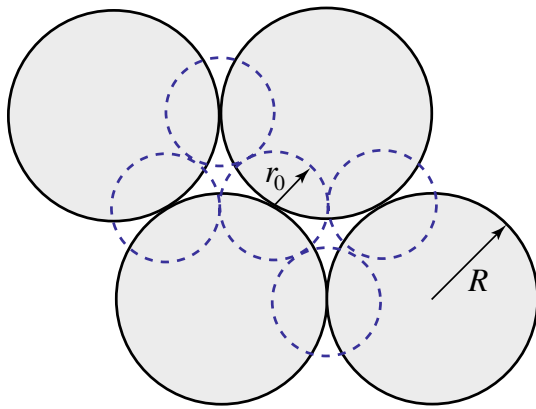


Fig. 1 Illustration of the solid grains with radius R (gray-shaded disks) and the localization spheres with radius r_0 (dashed blue circles) centered at grain–grain contacts

generated by the impact at $x = 0$ do not reach the right boundary over the time of interest. Thus, the boundary conditions at $x = L$ are taken to be zero Neumann conditions for all variables.

2.2 Grain-scale equations

The grain-scale model, described in detail in Gonthier [1], assumes an idealized structure consisting of a collection of identical spherical grains, each of radius R , packed into a configuration in which each grain is in contact with ϕ other grains. The geometry is illustrated in Fig. 1. At each macro-scale position x and time t , the entire grain volume per unit total volume, given by the volume fraction $\alpha(x, t)$, is distributed among a collection of *localization spheres* based upon the number density and the number of contact points per grain. The radius r_0 of the localization spheres (denoted by dashed blue circles in the figure) then emerges as

$$r_0 = R \left(\frac{\phi}{2} \right)^{-\frac{1}{3}}. \quad (10)$$

All of the localization spheres at a given x are assumed to behave in the same way, thereby allowing us to focus on one localization sphere at every x position of the bulk scale. Each localization sphere will be the site of energy deposition due to compaction and subsequent chemical reaction.

Figure 2 shows the geometry of a representative localization sphere. It is assumed that upon loading, the spherical grains undergo plastic deformation in the vicinity of each contact point and a contact disk of radius r_c is formed at the interface between the contacting grains. The radius of the contact disk is determined by the strength of the grain material and the loading. The energy from compaction is assumed to be deposited within a sphere of radius r_c , which will be

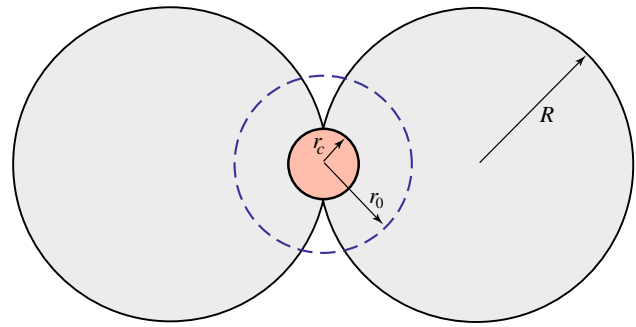


Fig. 2 Illustration of plastic deformation at a grain–grain contact. An energy-deposition sphere of radius r_c (red-shaded disk) occurs within its associated localization sphere of radius r_0 (dashed blue circle)

referred to as the *energy-deposition sphere*. In the present model both r_0 and r_c are taken to be constants.

The behavior at the grain scale within a localization sphere, $0 < r < r_0$, and for a bulk-scale position x , is modeled by a system of reaction–diffusion equations for the grain-scale temperature $\hat{T}(r, x, t)$ and reaction progress $\hat{\lambda}(r, x, t)$, with hats denoting grain-scale quantities. It is assumed that the grain-scale system advects with the bulk-scale velocity, diffusion of heat but not of the reactant is admitted, and Arrhenius kinetics governs the reaction rate. The evolution equations are

$$\rho C_v \frac{d\hat{T}}{dt} = \frac{k}{r^2} \frac{\partial}{\partial r} \left(r^2 \frac{\partial \hat{T}}{\partial r} \right) + \rho q (1 - \hat{\lambda}) \hat{\mathcal{R}}(\hat{T}) + \rho \hat{\mathcal{S}}, \quad (11)$$

$$\frac{d\hat{\lambda}}{dt} = (1 - \hat{\lambda}) \hat{\mathcal{R}}(\hat{T}), \quad (12)$$

where the bulk-scale material derivative is

$$\frac{d}{dt} = \frac{\partial}{\partial t} + u \frac{\partial}{\partial x}.$$

The Arrhenius reaction rate in the grain-scale equations is

$$\hat{\mathcal{R}}(\hat{T}) = z \exp(-T_a/\hat{T}), \quad (13)$$

where z is an Arrhenius prefactor and T_a is an activation temperature. The reaction–diffusion equation in (11) involves the bulk-scale density $\rho(x, t)$, the specific heat C_v and heat release q (defined previously and taken to be constants) and the thermal conductivity k of the solid grains (also taken to be constant). The energy from the bulk scale is determined by the power source term $\hat{\mathcal{S}}$, and this provides a coupling with the bulk scale as discussed in the next section.

The initial conditions for the grain-scale variables are $\hat{T} = T_0$ and $\hat{\lambda} = 0$. The heat flux at the boundaries of the localization spheres is assumed to be zero so that

$$\frac{\partial \hat{T}}{\partial r} = 0, \quad \text{at } r = 0 \text{ and } r_0. \tag{14}$$

Formally, no boundary conditions are required at the piston face since $u = 0$ there; however, we impose symmetry conditions

$$\frac{\partial \hat{T}}{\partial x} = \frac{\partial \hat{\lambda}}{\partial x} = 0, \quad \text{at } x = 0,$$

following the boundary conditions employed at the bulk scale for numerical convenience. The right-hand boundary at $x = L$ is an inflow boundary since $u = -u_p < 0$, and we impose $\hat{T} = T_0$ and $\hat{\lambda} = 0$ there.

2.3 Coupling

The coupling between the bulk and grain scales involves an averaging of grain-scale quantities to determine the corresponding bulk-scale quantities, and a model for the energy deposition from the bulk scale to the grain scale as given by \hat{S} in (11). We begin by defining an average of a grain-scale quantity over a localization sphere, $0 < r < r_0$, namely

$$f(x, t) = \langle \hat{f}(r, x, t) \rangle \equiv \frac{3}{r_0^3} \int_0^{r_0} \hat{f}(r, x, t) r^2 dr, \tag{15}$$

where f and \hat{f} are generic quantities defined at the bulk and grain scales, respectively. Using (15), we set

$$\lambda(x, t) = \langle \hat{\lambda}(r, x, t) \rangle, \tag{16}$$

to determine the bulk-scale reaction progress in (8) in terms of the grain-scale reaction progress governed by (12).

We next consider an average of the grain-scale equations as a guide to our modeling choice for \hat{S} . Using (12) to eliminate the reaction term in (11) and then applying the average defined in (15), we obtain

$$\rho C_v \frac{d}{dt} \langle \hat{T} \rangle = \rho q \frac{d}{dt} \langle \hat{\lambda} \rangle + \rho \langle \hat{S} \rangle. \tag{17}$$

Making the further assumption that

$$T(x, t) = \langle \hat{T}(r, x, t) \rangle, \tag{18}$$

and using (16), the rate of energy balance in (17) becomes

$$\langle \hat{S} \rangle = C_v \frac{dT}{dt} - q \frac{d\lambda}{dt}. \tag{19}$$

We next apply the thermal equation of state in (9) and use a straightforward manipulation of the bulk-scale equations in (1)–(3) to express (19) in the form

$$\langle \hat{S} \rangle = \frac{p - \beta}{\alpha \rho} \frac{d\alpha}{dt} + \frac{p + \pi}{\rho^2} \frac{d\rho}{dt}. \tag{20}$$

The first term on the right-hand side of (20) is the average rate of energy due to compaction of the grains, while the second term is the average rate of energy due to compression. (The term due to compression does not appear in [1] due to the assumption of incompressibility made in that work.) We assume that the contribution from compaction is localized in our grain-scale model, and thus, we set

$$\hat{S} = \frac{\mathcal{S}_\alpha r_0^3}{r_c^3} H(r_c - r), \tag{21}$$

where H is the Heaviside function and \mathcal{S}_α is the bulk-scale rate of energy deposition due to compaction given by

$$\mathcal{S}_\alpha = \frac{p - \beta}{\alpha \rho} \frac{d\alpha}{dt} = \frac{p - \beta}{\alpha \rho} \mathcal{F},$$

using (4). We note that $\langle \hat{S} \rangle = \mathcal{S}_\alpha$ according to (21) so that our model assumes that all of the bulk-scale compaction energy is deposited uniformly into the grain scale over the energy-deposition sphere $0 < r < r_c$. The remaining energy in (20) due to compression is not localized at the grain scale, and it is accounted for by applying the constraint on temperature in (18) as a uniform projection of the grain-scale temperature over the whole localization sphere $0 < r < r_0$. This projection is discussed further in Sect. 4.

3 Model parameters and dimensionless equations

For our multiscale model, we consider a representative explosive whose ambient state is taken to be

$$\alpha_0 = 0.8, \quad \rho_0 = 1900 \text{ kg/m}^3, \quad p_0 = 7.6 \text{ MPa}, \quad \lambda_0 = 0.$$

The constitutive parameters of the explosive material are assumed to be

$$\gamma = 5, \quad \pi = 3.4124 \times 10^9 \text{ Pa}, \quad q = 5.95 \times 10^6 \text{ J/kg}, \\ C_v = 1500 \text{ J/(kg K)},$$

and thus, the ambient temperature and sound speed have the values

$$T_0 = 300 \text{ K}, \quad c_0 = 3000 \text{ m/s}.$$

The value for the compaction viscosity in (5) is taken to be

$$\mu_c = 95.76 \text{ Pa s}.$$

The choices made above are the same as those used in [15] with the exception of the slightly lower value for the heat release q , so as to be more representative of practical explosives.

Additional quantities relevant to the grain scale, taken from [1], are the thermal conductivity

$$k = 0.502 \text{ J/(m s K)},$$

and the microstructure parameters

$$R = 2.5 \times 10^{-5} \text{ m}, \quad \phi = 12,$$

leading to

$$r_0 = 1.3758 \times 10^{-5} \text{ m}, \quad r_c = 3.4395 \times 10^{-6} \text{ m},$$

where (10) has been employed to determine r_0 and we have taken $r_c = r_0/4$. The reaction-rate parameters in (13), taken from [21], are

$$z = 2.8 \times 10^{11} \text{ s}^{-1}, \quad T_a = 1.79 \times 10^4 \text{ K}.$$

We choose to work with the problem in dimensionless form. To do this, we first select the reference quantities

$$t_{\text{ref}} = 10^{-6} \text{ s}, \quad \rho_{\text{ref}} = \rho_0, \quad u_{\text{ref}} = c_0, \quad T_{\text{ref}} = T_0, \quad r_{\text{ref}} = r_0,$$

for time, density, velocity, temperature and grain-scale length, respectively, and use these to define the additional reference quantities

$$p_{\text{ref}} = \rho_{\text{ref}} u_{\text{ref}}^2, \quad E_{\text{ref}} = u_{\text{ref}}^2, \quad x_{\text{ref}} = t_{\text{ref}} u_{\text{ref}},$$

for pressure, energy and bulk-scale length, respectively. We note that the reference lengths at the bulk and grain scales are chosen differently, while the reference time is the same for both scales. The governing equations are rendered dimensionless by setting $\psi' = \psi/\psi_{\text{ref}}$, where ψ is an independent or dependent variable in the equations and ψ' is its dimensionless counterpart, and by using the dimensionless parameters

$$\begin{aligned} \mu'_c &= \frac{\mu_c}{p_{\text{ref}} t_{\text{ref}}}, & \pi' &= \frac{\pi}{p_{\text{ref}}}, & q' &= \frac{q}{E_{\text{ref}}}, & \kappa' &= \frac{E_{\text{ref}}}{C_v T_{\text{ref}}}, \\ k' &= \frac{k t_{\text{ref}}}{\rho_{\text{ref}} C_v r_{\text{ref}}^2}. \end{aligned}$$

We also use the dimensionless grain-scale power source and reaction rate given by

$$\hat{S}' = \frac{\hat{S} t_{\text{ref}}}{E_{\text{ref}}}, \quad \hat{\mathcal{R}}' = \hat{\mathcal{R}} t_{\text{ref}} = \exp \left[T'_a \left(\frac{1}{T'_*} - \frac{1}{\hat{T}'} \right) \right],$$

Table 1 Reference quantities

Quantity	Value	Quantity	Value
t_{ref}	10^{-6} s	u_{ref}	3000 m/s
x_{ref}	$3 \times 10^{-3} \text{ m}$	ρ_{ref}	$17.1 \times 10^9 \text{ Pa}$
r_{ref}	$13.758 \times 10^{-6} \text{ m}$	E_{ref}	$9 \times 10^6 \text{ J/kg}$
ρ_{ref}	1900 kg/m^3	T_{ref}	300 K

Table 2 Dimensionless model parameters

Parameter	Value	Parameter	Value
q'	0.66111	μ'_c	0.0056
π'	0.19956	γ	5
κ'	20	k'	9.3056×10^{-4}
T'_a	59.67	T'_*	4.7571

where the dimensionless activation temperature and crossover temperature are given by

$$T'_a = \frac{T_a}{T_{\text{ref}}}, \quad T'_* = \frac{T'_a}{\ln(z t_{\text{ref}})}.$$

For large activation temperatures, the crossover temperature T'_* in the Arrhenius factor acts as a cutoff, reducing the reaction rate to negligible levels for $T' < T'_*$. The reference quantities are collected in Table 1, and the dimensionless parameters are given² in Table 2.

The dimensionless equations at the bulk scale have the same form as the original equations in (1)–(4), while the thermal equation of state in (9) assumes the form

$$T' = \kappa' \left(e' - \frac{\pi'}{\rho'} + q' \lambda \right), \quad (22)$$

and the grain-scale equations in (11) and (12) become

$$\begin{aligned} \frac{\partial \hat{T}'}{\partial t'} + u' \frac{\partial \hat{T}'}{\partial x'} &= \frac{k'}{\rho' r'^2} \frac{\partial}{\partial r'} \left(r'^2 \frac{\partial \hat{T}'}{\partial r'} \right) \\ &+ \kappa' \left(q' (1 - \hat{\lambda}) \hat{\mathcal{R}}'(\hat{T}') + \hat{S}' \right), \end{aligned} \quad (23)$$

$$\frac{\partial \hat{\lambda}}{\partial t'} + u' \frac{\partial \hat{\lambda}}{\partial x'} = (1 - \hat{\lambda}) \hat{\mathcal{R}}'(\hat{T}'). \quad (24)$$

² The values of the diffusivity k' and the activation temperature T'_a appearing in Table 2 are based upon data reported in the literature but produce a system that is much too stiff to be computationally feasible. We have therefore opted for a larger diffusivity and a smaller activation temperature for our computations, making sure that our choices do not alter the value of the planar flame speed. These choices are $T'_a = 33$ and $k' = 0.03$. The smaller activation temperature reduces stiffness, while the larger diffusivity broadens the flame, thereby rendering it more amenable to accurate numerical resolution.

We now drop the primes on the dimensionless variables and parameters in the subsequent sections of the paper for notational convenience.

4 Numerical method

In this section we describe the numerical approach used to solve the evolution equations governing the multiscale model. At the grain scale, the equations in (23) and (24) determine the evolution of the temperature \hat{T} and reaction progress $\hat{\lambda}$ as functions of the radial distance r within the localization sphere, the bulk-scale distance x , and the time t . We begin by introducing a uniform grid in the r -direction and setting

$$\begin{aligned} \tilde{T}_i(x, t) &= \hat{T}(r_i, x, t), \quad \tilde{\lambda}_i(x, t) = \hat{\lambda}(r_i, x, t), \\ i &= 0, 1, \dots, N_r + 1, \end{aligned}$$

where $r_i = (i - 1/2)h$ and $h = 1/N_r$. In terms of the vectors $\tilde{\mathbf{T}}(x, t) = (\tilde{T}_1, \dots, \tilde{T}_{N_r})^T$ and $\tilde{\boldsymbol{\lambda}}(x, t) = (\tilde{\lambda}_1, \dots, \tilde{\lambda}_{N_r})^T$, the discretized equations corresponding to (23) and (24) have the form

$$\frac{\partial}{\partial t} \tilde{\mathbf{T}} + u \frac{\partial}{\partial x} \tilde{\mathbf{T}} = \frac{k}{\rho} \mathcal{L}_h(\tilde{\mathbf{T}}) + \kappa \left(q \mathbf{R}(\tilde{\boldsymbol{\lambda}}, \tilde{\mathbf{T}}) + \hat{\mathcal{S}}(\alpha, \rho, p) \right), \tag{25}$$

$$\frac{\partial}{\partial t} \tilde{\boldsymbol{\lambda}} + u \frac{\partial}{\partial x} \tilde{\boldsymbol{\lambda}} = \mathbf{R}(\tilde{\boldsymbol{\lambda}}, \tilde{\mathbf{T}}), \tag{26}$$

where \mathcal{L}_h is a centered second-order accurate approximation of the diffusion operator, \mathbf{R} is the reaction term, and $\hat{\mathcal{S}}$ is the power source term, which depends on the volume fraction, density, and pressure of the solid at the bulk scale according to (21). Second-order accurate approximations of the no-flux boundary conditions in (14) are $\tilde{T}_0 = \tilde{T}_1$ and $\tilde{T}_{N_r+1} = \tilde{T}_{N_r}$, and these have been used to eliminate the ghost values at $i = 0$ and $i = N_r + 1$, respectively, from (25). Also, we include an ignition-temperature threshold to the reaction term, \mathbf{R} , so that the i th component of the reaction term is set to zero if $\tilde{T}_i < T_{\text{ign}}$, where $T_{\text{ign}} = 1.05$ is a value slightly greater than the (dimensionless) ambient value, $T_0 = 1$.

The bulk-scale equations in (1)–(4) may now be combined with the grain-scale equations in (25) and (26) to give a system of equations of the form

$$\frac{\partial \mathbf{u}}{\partial t} + \frac{\partial}{\partial x} \mathbf{f}(\mathbf{u}) = D(\mathbf{u}) \frac{\partial \mathbf{u}}{\partial x} + \mathbf{k}(\mathbf{u}), \tag{27}$$

where

$$\begin{aligned} \mathbf{u} &= \begin{bmatrix} \alpha \rho \\ \alpha \rho u \\ \alpha \rho E \\ \alpha \\ \tilde{\mathbf{T}} \\ \tilde{\boldsymbol{\lambda}} \end{bmatrix}, \quad \mathbf{f}(\mathbf{u}) = \begin{bmatrix} \alpha \rho u \\ \alpha (\rho u^2 + p) \\ \alpha u (\rho E + p) \\ 0 \\ \mathbf{0} \\ \mathbf{0} \end{bmatrix}, \\ D(\mathbf{u}) &= \begin{bmatrix} 0 & & & & & \\ & 0 & & & & \\ & & 0 & & & \\ & & & -u & & \\ & & & & -uI & \\ & & & & & -uI \end{bmatrix}, \\ \mathbf{k}(\mathbf{u}) &= \begin{bmatrix} 0 \\ 0 \\ 0 \\ \mathcal{F}(\mathbf{u}) \\ k \mathcal{L}_h(\tilde{\mathbf{T}})/\rho + \kappa (q \mathbf{R}(\tilde{\boldsymbol{\lambda}}, \tilde{\mathbf{T}}) + \hat{\mathcal{S}}(\alpha, \rho, p)) \\ \mathbf{R}(\tilde{\boldsymbol{\lambda}}, \tilde{\mathbf{T}}) \end{bmatrix}. \end{aligned}$$

and I is the $N_r \times N_r$ identity. Here, $\mathbf{f}(\mathbf{u})$ contains the conservative components of the flux at the bulk scale, $D(\mathbf{u}) \partial_x \mathbf{u}$ is the nonconservative advection term, and $\mathbf{k}(\mathbf{u})$ is a source term involving grain-scale diffusion, reaction, and the localized power source at the grain scale due to bulk-scale compaction. The evolution equations in (27) are to be solved subject to the coupling constraints

$$\begin{aligned} \lambda(x, t) &= \langle \tilde{\boldsymbol{\lambda}} \rangle_h \equiv 3 \sum_{i=1}^{N_r} \tilde{\lambda}_i(x, t) r_i^2 h, \\ T(x, t) &= \langle \tilde{\mathbf{T}} \rangle_h \equiv 3 \sum_{i=1}^{N_r} \tilde{T}_i(x, t) r_i^2 h, \end{aligned} \tag{28}$$

which are second-order accurate approximations of the integral constraints in (16) and (18), respectively. The initial conditions and boundary conditions for (27) are taken from those discussed in Sects. 2.1 and 2.2.

The evolution governed by the first-order system in (27) is a mixture of nonlinear advection, stiff reaction and relatively weak diffusion that acts on the components of $\tilde{\mathbf{T}}$ at the grain scale. The general form of the system is similar to ones that have appeared in several of our previous papers, e.g., [14, 15, 22], and we follow a similar numerical approach based on a second-order, Strang-type splitting method which handles the nonlinear advection terms and the nondifferentiated source term in separate steps. The time-stepping scheme has the form

$$\mathbf{U}_j^{n+1} = S_k(\Delta t/2) S_h(\Delta t) S_k(\Delta t/2) \mathbf{U}_j^n, \tag{29}$$

where \mathbf{U}_j^n is an approximation of the cell average of $\mathbf{u}(x, t)$ on a uniform grid $x_j = j\Delta x$ at a time t_n , and Δt is the time step from t_n to t_{n+1} . The operators $S_h(\Delta t)$ and $S_k(\Delta t/2)$ represent numerical integrations of the equations

$$\frac{\partial \mathbf{u}}{\partial t} + \frac{\partial}{\partial x} \mathbf{f}(\mathbf{u}) = D(\mathbf{u}) \frac{\partial \mathbf{u}}{\partial x}, \quad (30)$$

and

$$\frac{\partial \mathbf{u}}{\partial t} = \mathbf{k}(\mathbf{u}), \quad (31)$$

over the time intervals Δt and $\Delta t/2$, respectively. A high-resolution extension of Godunov's method is used for the hyperbolic system in (30). This method treats both the conservative and nonconservative advection terms, and it follows the methods discussed in [14, 22]. Numerical integration of the source term in (31) uses a second-order accurate Runge–Kutta (RK) error-control scheme similar to the one discussed in [15]. A value for Δt is chosen at each time step according to a CFL stability condition. The RK integration may use sub-CFL time steps over the interval $\Delta t/2$, and the value for Δt is reduced at subsequent time steps if too many steps are taken (typically more than 4). Further details of these elements of the time-stepping scheme can be found in [27].

The coupling constraints in (28) are imposed after each application of the source operator, $S_k(\Delta t/2)$, in (29). The computed components of $\tilde{\lambda}$ determine the bulk-scale reaction progress λ following the averaging given in (28). The bulk-scale λ is then used in (8) and (22) to determine the bulk-scale internal energy and temperature, respectively. The bulk-scale temperature at this stage is not equal to the average of the computed grain-scale temperature, in general, since the contribution to the grain-scale power source in (20) due to bulk-scale compression has been omitted from $\tilde{\mathbf{S}}$ as discussed in Sect. 2.3. Thus, we regard the grain-scale temperature computed from $S_k(\Delta t/2)$ as a *predicted* temperature and denote it by $\tilde{\mathbf{T}}^p$. The temperature average in (28) is then used to *correct* the components of the predicted temperature by applying a uniform temperature projection over the grain scale according to the formula

$$\tilde{T}_i = \tilde{T}_i^p + \Delta T, \quad i = 1, 2, \dots, N_r, \quad \Delta T = T - \langle \tilde{\mathbf{T}}^p \rangle_h, \quad (32)$$

for all grid cells x_j at the bulk scale. This temperature adjustment accounts for the nonlocalized power source imposed on the temperature at the grain scale due to bulk-scale compression, $\Delta T > 0$, or expansion, $\Delta T < 0$.³

³ In practice, we also apply the projection in (32) after the subsequent hydro step, $S_h(\Delta t)$, to account for convection of the bulk-scale temperature.

Solutions of the model equations possess discontinuities at shocks and contacts, as well as thin layers in which reaction and compaction are important. We use a scheme of adaptive mesh refinement (AMR) in order to increase the grid resolution in x and t near these thin structures. The basic approach follows that discussed in [15] for two-phase reactive flow in one space dimension, which is a special case of the more general multidimensional AMR schemes described in [23–26]. Each simulation has a base grid covering the domain $x \in [0, L]$ with $\Delta x_1 = L/N_x$, where N_x is the number of grid cells of the base grid. As the solution evolves in time, grids at finer levels of refinement may be added into the AMR-system in order to increase the resolution where the solution is changing rapidly in either space or time. (Fine grids may also be removed if the solution is sufficiently resolved on coarser grids.) Thin layers in space are detected by flagging cells where the magnitude of the second undivided difference of the components of \mathbf{U}_j^n is larger than a tolerance. Rapid temporal variations are flagged by monitoring the number of sub-CFL time steps needed for the integration of the source term. Once all the cells have been checked, refinement grid patches are created over the flagged cells. We use a refinement factor of $n_r = 4$ for all calculations and a maximum of ℓ_{\max} refinement levels, where $\ell_{\max} = 3$ typically. We note that layers also exist in the grain-scale direction balancing diffusion and reaction, but these layers (i.e., flames) are resolved without AMR using a sufficiently fine grid in the r -direction.

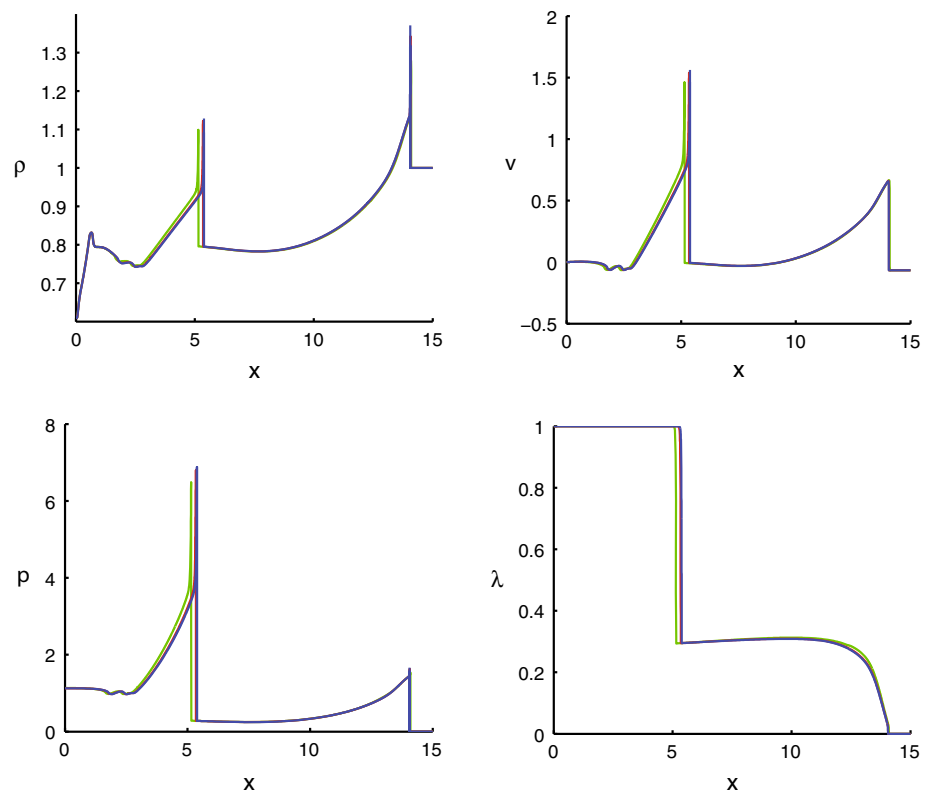
5 Verification

The convergence of numerical solutions on the AMR-grid system may be judged by comparing solutions using a fixed grid spacing on the base grid, $\Delta x_1 = 1/500$, with increasing values of ℓ_{\max} to systematically increase the effective grid resolution. Of particular interest is the behavior of the solution near thin-layered structures, such as compaction layers, shocks and reaction zones, as well as the behavior in smooth regions of the flow structure. Figure 3 shows profiles of the bulk-scale density, velocity, pressure, and reaction progress at $t = 8$ for varying choices of ℓ_{\max} between 1 and 3. The (dimensionless) upstream conditions are given by

$$\alpha_0 = 0.8, \quad \rho_0 = 1, \quad u_0 = -0.0667, \\ p_0 = 4.444 \times 10^{-4}, \quad \hat{T}_0 = 1, \quad \hat{\lambda}_0 = 0,$$

with the reaction, diffusion, and equation of state parameters provided in Table 2. The initial velocity corresponds to a piston velocity of 200 m/s. The number of grain-scale grid points used is $N_r = 160$ for all values of ℓ_{\max} . The compaction layer near $x = 14$ is well resolved for all three values of ℓ_{\max} , while the primary reaction zone near $x = 5$ is well

Fig. 3 Profiles of bulk-scale density, velocity, pressure, and reaction progress at $t = 8$ for $\ell_{\max} = 1$ (green curves), 2 (red), and 3 (blue). All solutions use a base grid with $\Delta x_1 = 1/500$ and a grain-scale grid with $N_r = 160$



resolved on the finest two grid resolutions, $\ell_{\max} = 2$ and 3. The convergence behavior shown in Fig. 3 is representative of a developing detonation for the multiscale model.

In order to examine the convergence behavior for different resolutions at the grain scale, the calculations above are repeated with ℓ_{\max} held fixed at a value of 3, but with $N_r = 40, 80,$ and 160. Figure 4 shows the behavior of the bulk-scale density, velocity, pressure, and reaction progress at $t = 8$ for the same initial conditions and parameters used for the convergence study shown in Fig. 3. As before, we note excellent agreement of the profiles for the highest two resolutions indicating that the grain-scale is sufficiently resolved to accurately determine the bulk-scale behavior.

The subsequent calculations presented in Sect. 6 use the same value of Δx_1 along with $\ell_{\max} = 3$ and $N_r = 160$.

6 Results

The aim of this investigation is to examine the evolutionary behavior of the model under study, with emphasis on the mechanics of formation and propagation of detonation structures. A number of studies were conducted to explore the dependence of the evolutionary process on system parameters. We have chosen to focus on two parameters in particular, the crossover temperature T^* and the diffusivity k , the former representing chemical kinetics and the latter thermal trans-

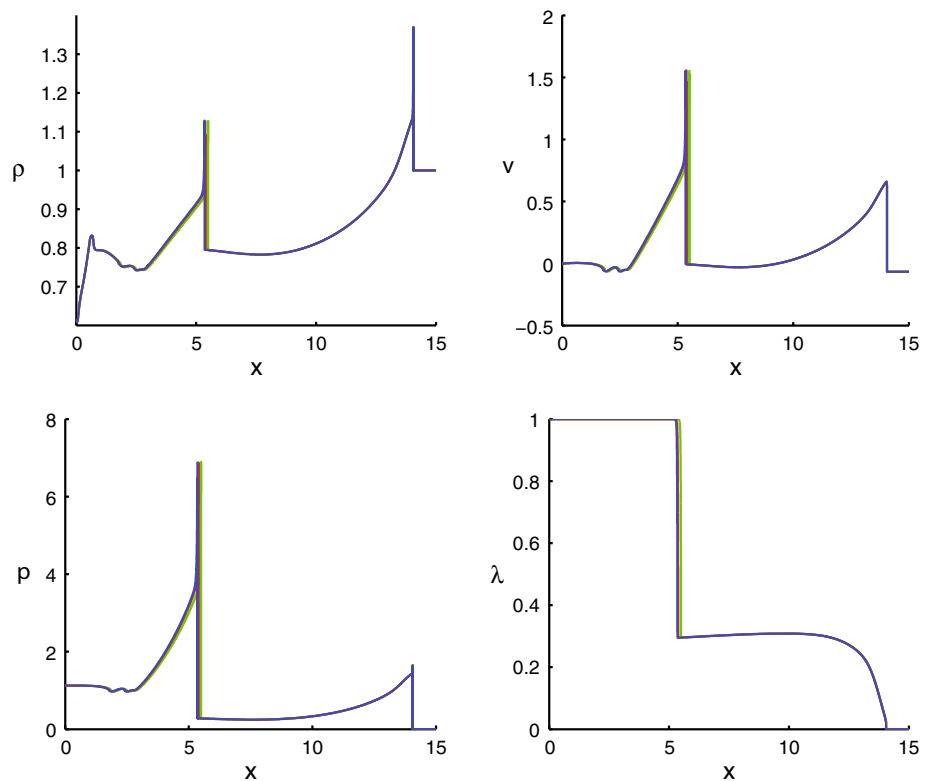
port at the grain scale. The results are first described in detail for Case 1, a base case corresponding to the representative set of system parameters listed in Table 2. The results for this case are followed by briefer descriptions of the results for two other cases, Case 2 corresponding to a lower value of T^* and Case 3 to a smaller value of k .

6.1 Case 1: Base case

6.1.1 Formation and propagation of the initial reaction wave, Case 1

We begin with a description of the early-time evolution at the bulk scale, with the relevant profiles displayed in Fig. 5. Following impact, passage of the piston-driven shock compacts the material behind it to an increasing degree, even as the shock itself loses strength due to energy transfer to the grain scale. The shock disappears altogether by $t = 0.4$ as evident in the profiles of pressure, density, and temperature. Temperature increases gradually behind the wavehead but more rapidly near the piston face which is also the site of strongest reactant consumption. This rise in temperature is accompanied by an increase in pressure and a drop in density. Thus, the material, after having experienced a small amount of compression immediately behind the wavehead, expands at the rear of the wave. We shall see that this expansion has a significant influence on the events at the grain scale. We note that

Fig. 4 Profiles of bulk-scale density, velocity, pressure and reaction progress at $t = 8$ for a grain-scale grid with $N_r = 40$ (green curves), 80 (red), and 160 (blue). All solutions use a base grid with $\Delta x_1 = 1/500$ and $\ell_{\max} = 3$



the leading edge of the reaction zone continues to lag behind the wavehead. By $t = 0.8$ the temperature increase behind the wavehead has accelerated, accompanied by stronger reactant consumption and faster increases in pressure and density at the same location. By $t = 1$ this feature has become more pronounced, causing the profiles to steepen further. It is noteworthy that the highest bulk temperature of about 2.4 is still significantly below the crossover temperature $T^* = 4.75$, so that the reaction seen at the bulk scale at these early times is the result of heating not at the bulk scale but at the grain scale, as we now show.

The grain-scale events at $t = 1$ are captured in Fig. 6 in the contours of grain-scale reaction progress $\hat{\lambda}$ and grain-scale temperature \hat{T} . In these contour plots, drawn in the x - r plane, $\hat{\lambda}$ ranges from 0 to 1 and \hat{T} from 0 to 20. The plots show that when the compaction wave passes over a grain at location x , it deposits compaction energy in the region $r \in [0, r_c]$ where $r_c = 0.25$. The temperature in this region rises to a value above the crossover temperature, creating a hot spot in which vigorous reaction is initiated. This results in the creation of a flame front, essentially an interface between the unreacted and fully reacted sections of the grain, that advances into the region $r > r_c$. The farther behind the wavehead an x -location is, the farther in r the flame has advanced. (Corresponding plots at earlier times show similar features and are therefore not displayed.) The plots at $t = 1$ show three other noteworthy features. First, the flame is hottest at the wave-

head but becomes progressively cooler at locations farther behind the wavehead. The reason is the bulk-scale expansion alluded to above, which applies uniformly across the grains. Second, at $x = 0$, $\lambda < 0.5$ (see Fig. 5) but $\hat{\lambda}(0, r, 1) = 1$ for $r \in [0, 0.6]$. This seeming disparity is due to the contribution of geometry in the computation of the bulk-scale average of a grain-scale quantity. Third, near the piston there is a hint of the flame slowing down. We examine this feature in some detail by focusing on the radial profiles of $\hat{\lambda}$, \hat{T} , and the grain-scale reaction rate at the piston face, $x = 0$. The evolution of these profiles is displayed in Fig. 7.

Figure 7a shows that as time increases from $t = 0.2$ to $t = 1.0$, the flame travels radially outward from the energy-deposition region, losing both strength and speed as it does so. Profiles of $\hat{\lambda}$ attest to the loss in flame speed, while the loss in strength is evident in the profiles of the temperature and the reaction rate. Figure 7b displays profiles from $t = 2.0$ to $t = 3.5$ wherein the flame stands still, weakening further as heat is lost from the burned to the unburned side of the flame. Profiles from $t = 4.5$ to $t = 6.0$, shown in Fig. 7c, demonstrate that heat transferred to the unburned side by diffusion has raised the temperature on that side sufficiently to spur reaction there. The resulting energy release accelerates the reaction and raises the temperature of the previously unburned region still further to the extent that the direction of heat transfer is reversed. In fact the profiles in Fig. 7d, from $t = 6.5$ to $t = 7.0$, point to a *flame rever-*

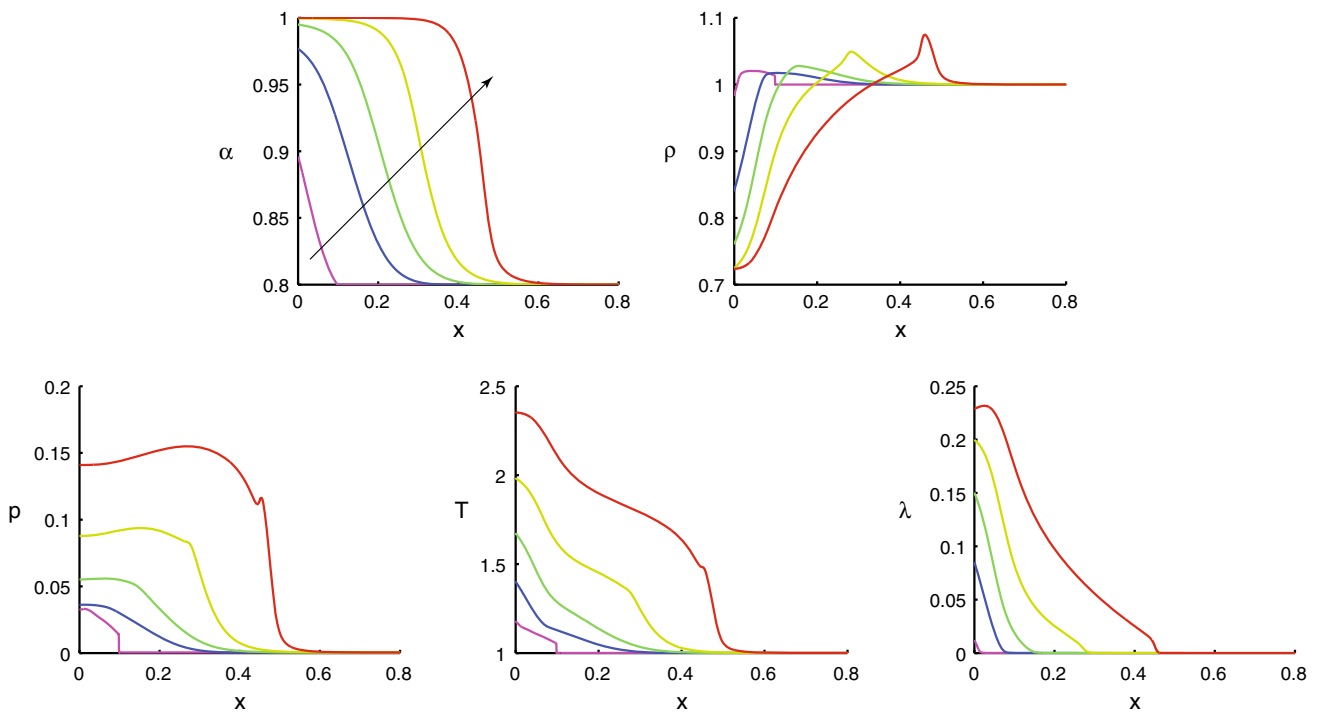


Fig. 5 The formation of the initial reaction wave for Case 1. Profiles of volume fraction, density, pressure, temperature, and reaction progress at $t = 0.1, 0.4, 0.6, 0.8,$ and 1.0 . The arrow indicates passage of time

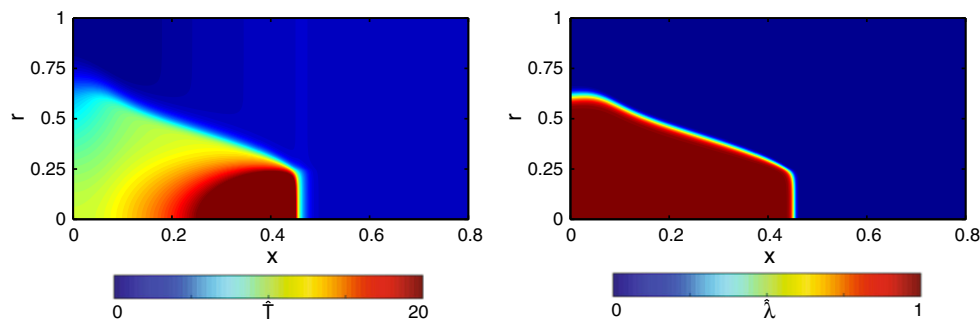


Fig. 6 Contour plots of the grain-scale variables \hat{T} (left) and $\hat{\lambda}$ (right) at $t = 1$ for Case 1

sal, i.e., a flame traveling radially inward from the boundary $r = 1$ to rapidly consume the pocket of the yet unburned reactant.

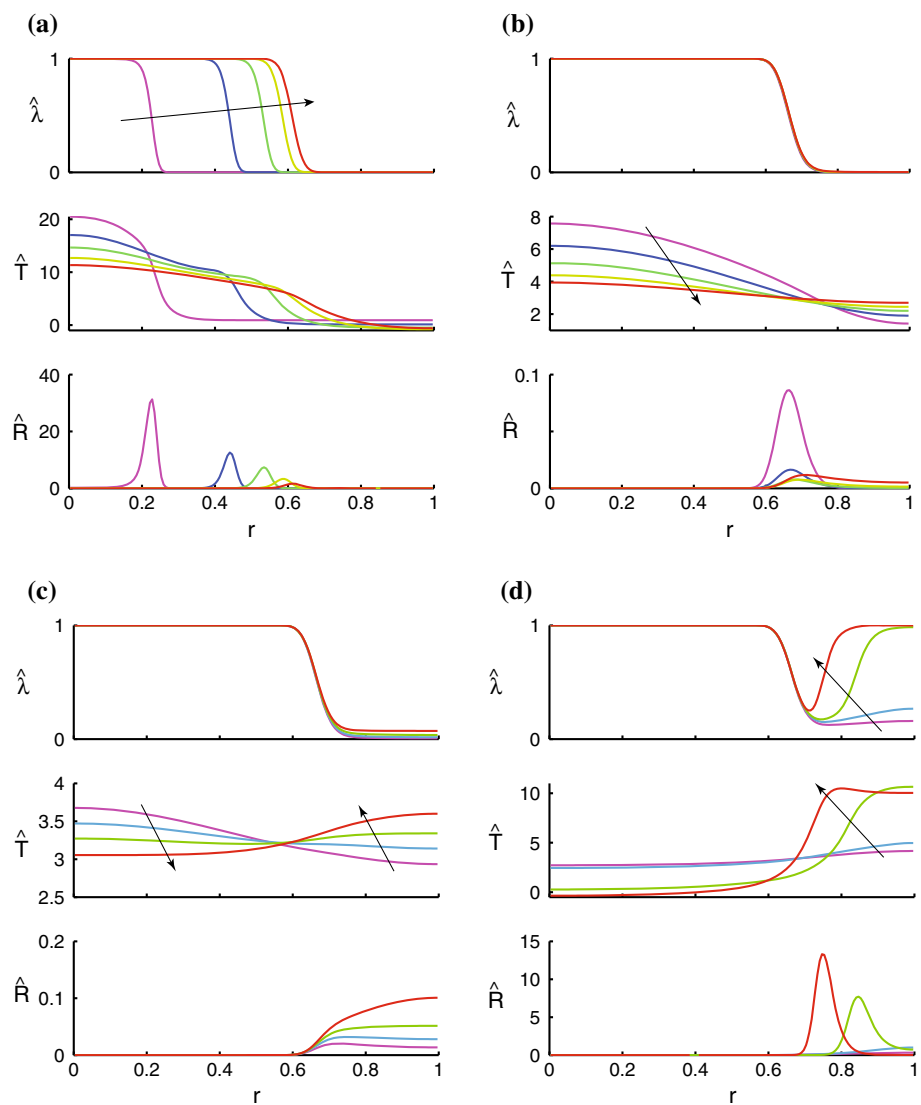
We now turn to Fig. 8, which shows the states of the grain-scale and the bulk-scale systems at $t = 4.0$. The bulk-scale wave, which had shown signs of steepening as early as $t = 1$, has now developed a shock, L_1 , at the wavehead, with a correspondingly thin compaction zone. At the grain scale, the flame immediately behind the wavehead is just at the edge of the energy-deposition region there, but at locations further behind the wavehead the flame has advanced radially outward. Except for a discernible region behind and close to the wavehead, the radial advance of the flame is more or less uniform at all x -locations within the wave, a result of the expansion-induced cooling of the flame back toward the piston, discussed earlier. We note that throughout the wave

a broad swath of unreacted material persists near the outer radial boundary, $r = 1$.

6.1.2 Formation and propagation of the secondary reaction wave: Case 1, Cycle 1

The situation at $t = 7.0$ is shown in Fig. 9 and is best understood in conjunction with Fig. 7d. We note that at the piston face the consumption of the unreacted pocket near $r = 1$ by the reverse flame, shown in Fig. 7d, has led to a local increase in the grain-scale temperature, which in turn has contributed to the appearance of local peaks in the bulk-scale quantities near $x = 0$. Thus, a secondary wave is born near the piston as the lead shock continues its advance. Figure 10, corresponding to $t = 7.1$ and drawn on a magnified horizontal scale, shows that this secondary wave quickly develops into

Fig. 7 Flame quenching and rebirth at the piston face for Case 1. Profiles of $\hat{\lambda}$, \hat{T} , and grain-scale reaction rate \hat{R} at **a** $t = 0.2, 0.4, 0.6, 0.8,$ and 1.0 ; **b** $t = 2.0, 2.54, 3.0,$ and 3.5 ; **c** $t = 4.5, 5.0, 5.5,$ and 6.0 ; and **d** $t = 6.5, 6.7, 6.9,$ and 7.0 . Arrows indicate progression of time



a shock, A_1 , which moves rapidly into the partially reacted region identified above and heats it to a temperature significantly above the crossover temperature. A vigorous reaction ensues and the hitherto unreacted material is rapidly consumed, before reverse flames of the kind discussed above have had the opportunity to do so. The secondary shock is now located at $x = 0.63$. Behind this shock, between $x = 0.1$ and $x = 0.4$, there is a remnant of partially reacted material. The secondary shock was too weak when it traversed this section, but became strong beyond the leading edge of the section to initiate the uniform reaction now seen immediately behind the shock.

6.1.3 Formation and propagation of the secondary reaction wave: Case 1, Cycle 2

Profiles of bulk-scale reaction progress and pressure displayed in Fig. 11 for times ranging from $t = 7.0$ to $t = 10.0$

show that the secondary shock A_1 , passing through material already processed by the lead shock L_1 , separates fully reacted material behind it from partially reacted material in front of it, and is stronger than, and travels faster than, the lead shock. The two shocks collide around $t = 10.9$, and the collision event is shown in the profiles of bulk-scale pressure, reaction progress and temperature displayed in Fig. 12. The collision generates three waves, a weak and barely discernible reflected shock traveling backward, a shock L_2 transmitted into the ambient material, and a contact surface C_1 , all clearly evident in Fig. 12. It is now the contact surface that separates the fully reacted material behind it from the partially reacted material ahead of it and behind the transmitted shock. The bulk-scale profiles of Fig. 13 show the propagation of the transmitted shock L_2 over the period $t = 11.0$ to $t = 13.0$. Initially overdriven, the shock decays to settle at a fixed strength by around $t = 12.0$.

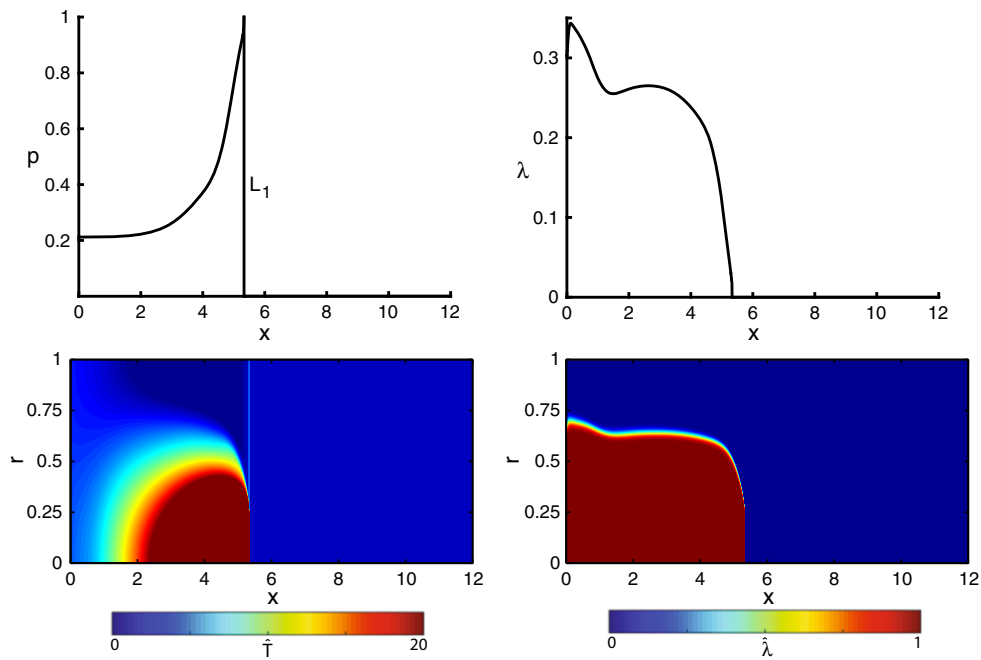


Fig. 8 Profiles for Case 1 of the bulk-scale quantities p and λ (top) and contour plots of the grain-scale variables \hat{T} (bottom left) and $\hat{\lambda}$ (bottom right) at $t = 4$

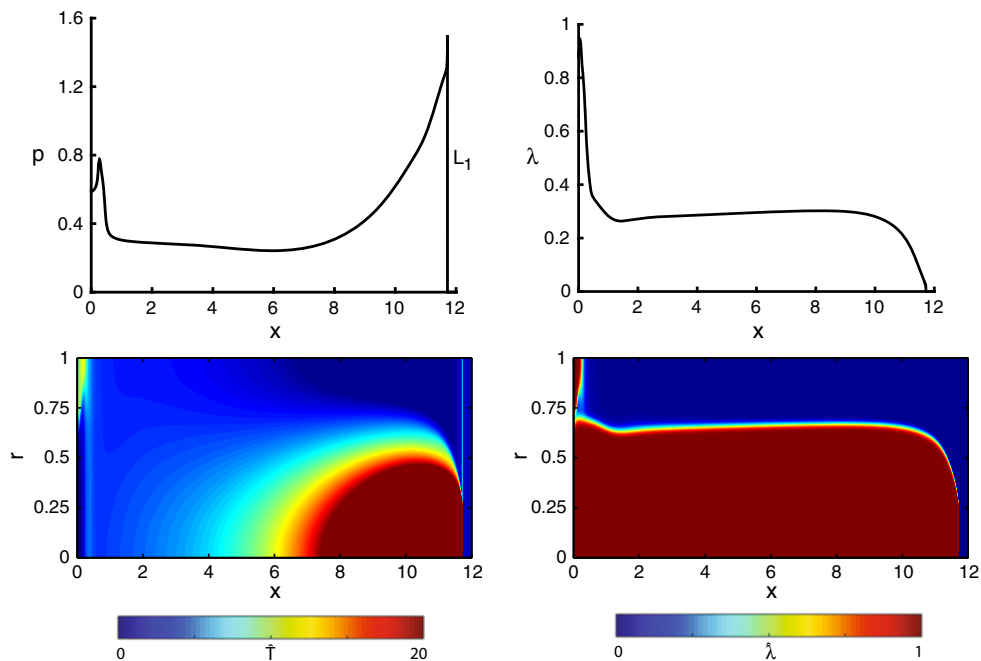


Fig. 9 Profiles for Case 1 of the bulk-scale quantities p and λ (top) and contour plots of the grain-scale variables \hat{T} (bottom left) and $\hat{\lambda}$ (bottom right) at $t = 7$

A combined portrait of grain-scale and bulk-scale quantities at $t = 13.0$ is displayed in Fig. 14. The contour plots in this figure show that between the now lead shock L_2 and the contact surface C_1 there exists a flame spreading radially outward at the grain scale. It is useful to contrast this flame with a similar flame that appeared at $t = 4.0$ in the region

between the lead shock and the piston, as seen in the corresponding contour plots of Fig. 8. At that early time, the flame was propagating into essentially unreacted material, whereas now the material, after having been processed by the stronger transmitted shock, has already experienced some reaction.

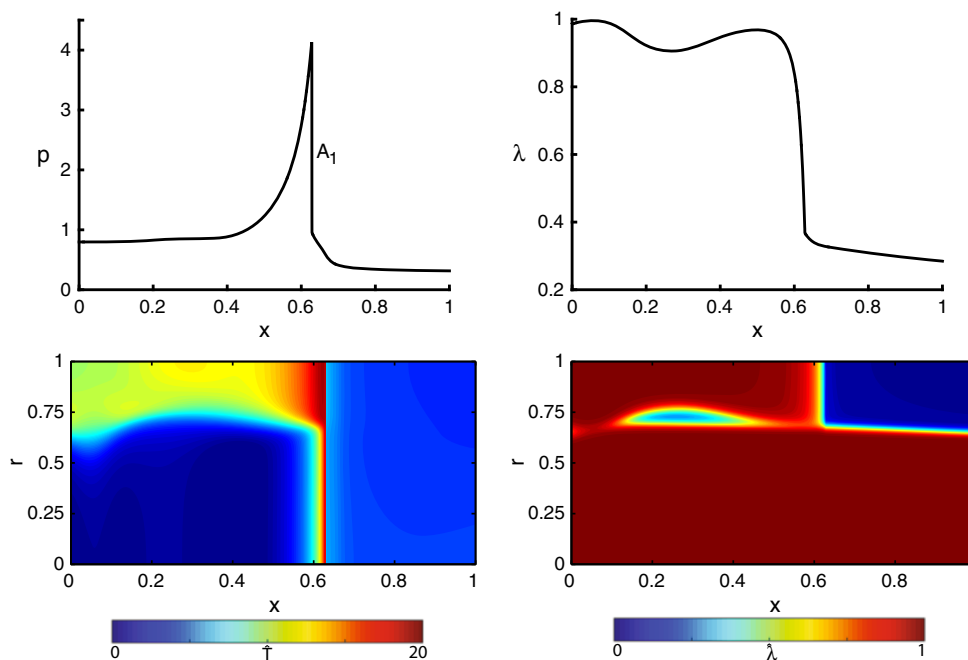


Fig. 10 Profiles for Case 1 of the bulk-scale quantities p and λ (top) and contour plots of the grain-scale variables \hat{T} (bottom left) and $\hat{\lambda}$ (bottom right) at $t = 7.1$, near the piston face

Fig. 11 The progression of the secondary reaction wave for Case 1. Profiles of pressure and reaction progress at $t = 7.0, 8.0, 9.0$, and 10.0

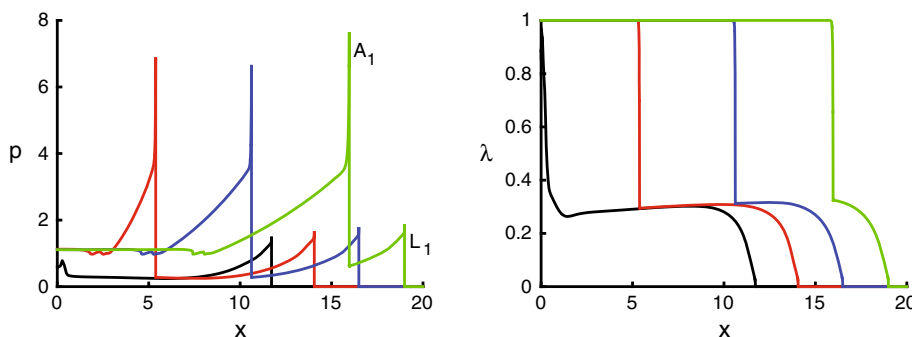
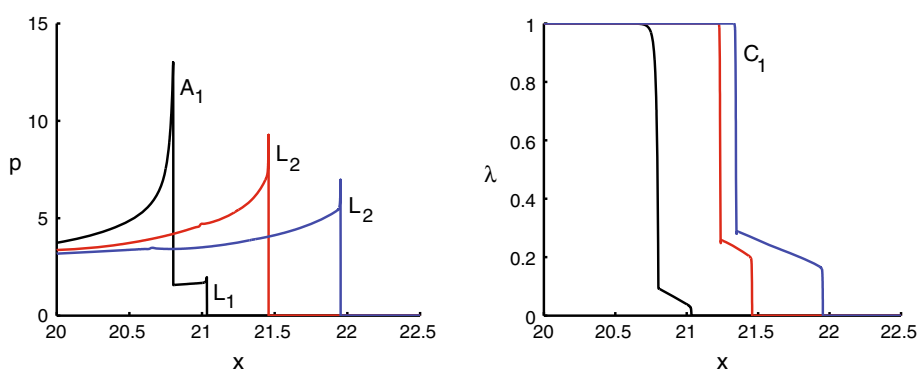


Fig. 12 The collision of the secondary reaction wave with the lead wave for Case 1. Profiles of pressure and reaction progress at $t = 10.8, 10.9$, and 11.0



The flame is now hotter and has travelled closer to the outer boundary $r = 1$.

The formation of a new secondary reaction zone immediately ahead of the contact is illustrated in Fig. 15, drawn for $t = 14.5$. The situation is analogous to that of the re-ignition of the quenched flame near the piston face at $t = 7.0$, dis-

played in Fig. 9. Such a quenched flame is now found in the vicinity of the contact. Diffusion transfers heat from the hot region behind the flame to the cold region ahead and in this case propels the flame forward, rather than creating the reverse flame seen in the earlier instance. This new secondary reaction zone creates a wave at the macro-scale which will

Fig. 13 The propagation of the transmitted shock for Case 1. Profiles of pressure and reaction progress at $t = 11.0, 12.0,$ and 13.0

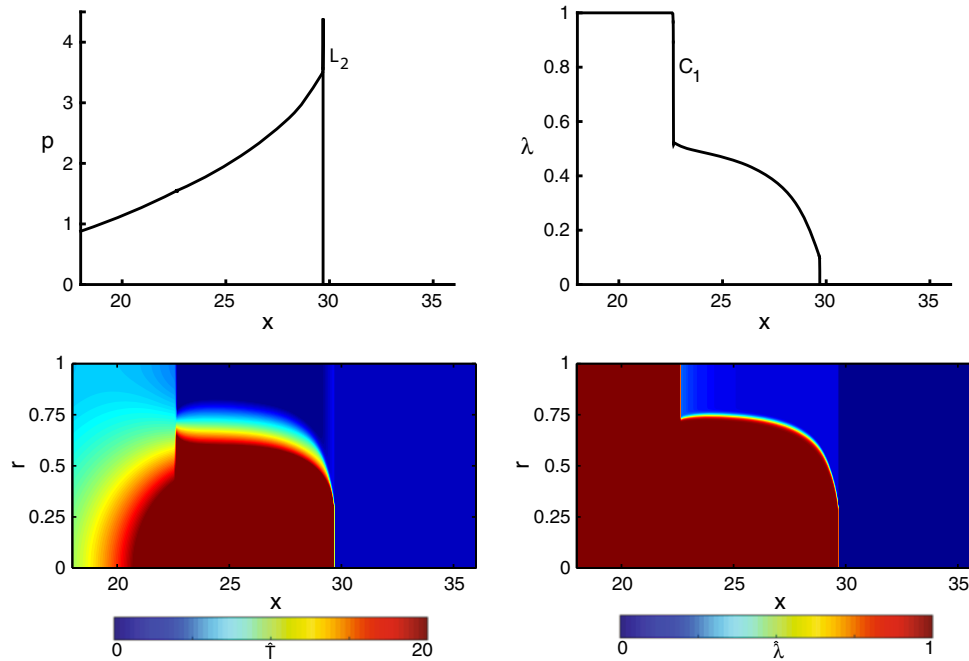
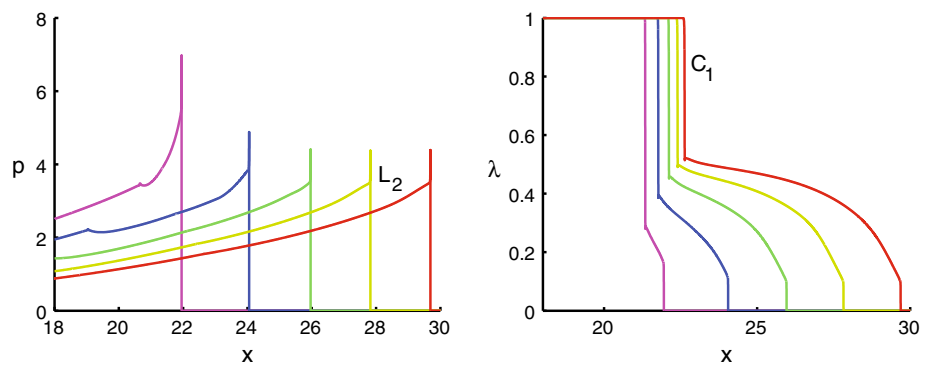


Fig. 14 Profiles for Case 1 of the bulk-scale quantities p and λ (top) and contour plots of the grain-scale variables \hat{T} (bottom left) and $\hat{\lambda}$ (bottom right) at $t = 13.0$

transition into another secondary detonation. This secondary detonation, once initiated, begins to consume the unreacted explosive left behind by the lead shock wave. Figure 16 shows the bulk pressure and grain-scale reaction progress at $t = 16$. We notice that the new secondary shock A_2 is again stronger and faster than the current lead shock L_2 due to the higher pressure ahead of this shock. The difference in shock speeds will eventually lead to the collision of the two shocks much in the same way as the earlier collision at time $t = 10.9$.

The new secondary shock is found to collide with the lead shock at $t = 17.6$, leading to the transmittal of yet another shock, L_3 , into the unreacted material. The process of a new secondary shock forming and then colliding with the new lead shock occurs repeatedly. The new secondary shock appears near but not at the contact wave and again overtakes the lead shock leading to another collision. Each time the shocks collide, the initial transmitted shock has a

larger maximum pressure. Figure 17 shows the density, pressure, reaction progress and temperature profiles at $t = 10.9, 17.7,$ and 24.8 . Each of these times immediately follows the formation of a transmitted shock. As evidenced by the pressure profile, each occurrence results in the new transmitted shock being stronger than the previous shock.

6.2 Case 2: Lower crossover temperature

We now examine the case where the crossover temperature T^* has been reduced to 4.0 from the base-case value of 4.75. This makes the explosive more reactive at lower temperatures. We shall find that the overall scenario following piston impact retains the repetitive character seen in Case 1: A zone of enhanced reaction appears behind the lead shock, giving rise to a new shock which overtakes and collides with the lead shock, thereby resulting in a faster and stronger trans-

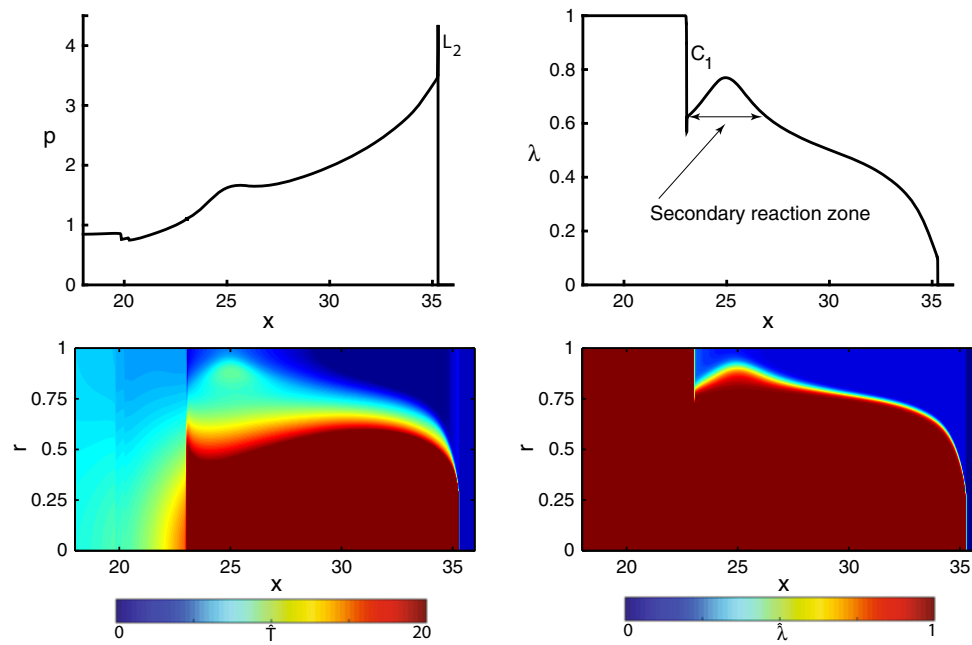


Fig. 15 Profiles for Case 1 of the bulk-scale quantities p and λ (top) and contour plots of the grain-scale variables \hat{T} (bottom left) and $\hat{\lambda}$ (bottom right) at $t = 14.5$

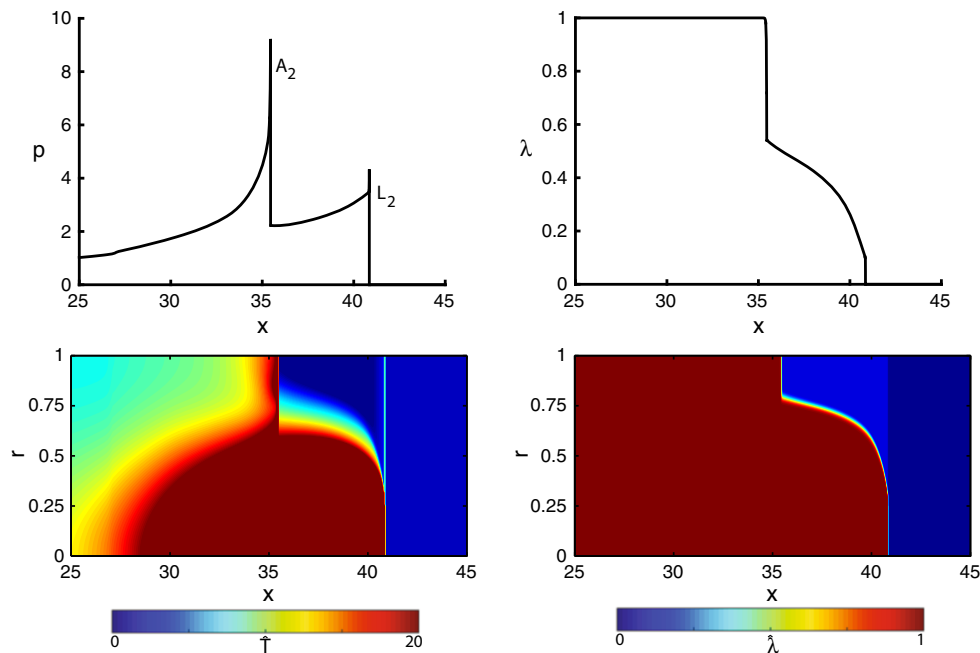


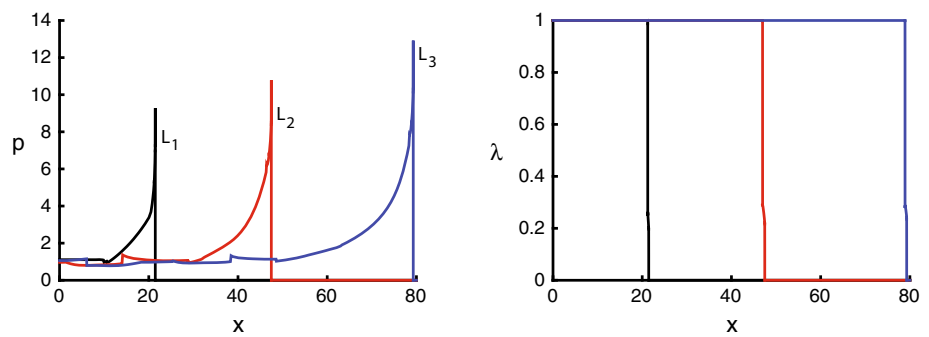
Fig. 16 Profiles for Case 1 of the bulk-scale quantities p and λ (top) and contour plots of the grain-scale variables \hat{T} (bottom left) and $\hat{\lambda}$ (bottom right) at $t = 16.0$

mitted shock which becomes the new lead shock for the next cycle. The details differ significantly, however, and it is on them that the discussion will chiefly be focused. We shall describe the events mostly by displaying bulk-scale profiles, resorting to grain-scale contour plots sparingly for additional clarification.

6.2.1 Formation and propagation of the initial reaction wave, Case 2

The early-time evolution at the bulk scale is displayed in the profiles gathered in Fig. 18. These profiles correspond to the same instants of time, $t = 0.1, 0.4, 0.6, 0.8,$ and 1.0 , as were

Fig. 17 The first three transmitted shocks for Case 1. Profiles at $t = 10.9$, 17.7 , and 24.8 of pressure and reaction progress



chosen for the base case in Fig. 5. The development is akin to that for the base case, but faster. The wavehead steepens into a shock (labeled L_1) sooner, the wave travels farther, the compaction zone is thinner, and the peaks in temperature, pressure, and reaction progress are all higher at the corresponding time levels. The profiles of density again show an expansion behind the shock. The contour plots of reaction progress and temperature at the grain scale, shown in Fig. 19 for $t = 1$, reveal that in the region between the piston and the wavehead, the flame has now propagated farther into the grain than it did for the base case illustrated in Fig. 6.

6.2.2 Formation and propagation of the secondary reaction wave: Case 2, Cycle 1

As the primary reaction wave headed by the shock L_1 advances, a secondary reaction zone begins to form between L_1 and the piston face. Its structure at the grain scale, as a flame advancing radially outward, is evident in the contour plots of $\hat{\lambda}$ and \hat{T} at $t = 2.0$ in Fig. 20. Its bulk-scale manifestation appears in the profiles of λ and p plotted from $t = 1.7$ to $t = 2.8$ in Fig. 21. The profiles in Fig. 21a show the buildup of reaction within the secondary zone and the broadening of the associated pressure pulse. The profiles in Fig. 21b show the left-traveling and right-traveling edges of the pulse steepening into shocks at $t = 2.0$ and $t = 2.1$, respectively. The left-traveling shock A_1 quickly strengthens as the reactant behind it is fully consumed. It collides with the piston and reverses direction, now losing strength as it traverses rightward through the fully reacted region it had just created. Meanwhile, shock B_1 at the right edge continues to grow at a slower pace, with only partial consumption of reactant occurring behind it. Also noteworthy in the pressure profile at $t = 2.2$ is the appearance of yet another right-traveling shock B_2 and the associated bump in the profile of λ . This shock, though relatively weak at this stage, will play an important role in later developments. The profiles in Fig. 21c show the reflected shock A_1 entering the region of partial consumption, consuming the reactant fully and thereby gaining strength. By $t = 2.4$ the reaction behind shock B_1 has also intensified sufficiently such that at this stage, both shocks are

followed by zones of complete reaction. At $t = 2.5$, shock B_1 has just collided with the comparatively weak lead shock L_1 . The result is a contact surface C_1 , a very weak reflected shock and a stronger transmitted shock L_2 which becomes the new lead shock. The profiles in Fig. 21d show L_2 to be losing strength as it advances into the ambient material. Reaction behind L_2 is now only partially complete, and there is a jump in λ across the contact surface. Meanwhile, shock A_1 overtakes shock B_2 just after $t = 2.6$, generating a reflected shock traveling leftward which we shall continue to label as B_2 . The transmitted shock, still labeled A_1 , continues its passage through the partially reacted pocket, weakening as it does so but fully consuming the pocket by $t = 2.8$. At this time, a state of complete reaction exists between the piston and the contact surface C_1 , and both shocks A_1 and L_2 are becoming weaker.

6.2.3 Formation and propagation of the secondary reaction wave: Case 2, Cycle 2

Figure 22a displays the profiles of pressure and reaction progress at times $t = 3.1$ to $t = 3.5$. At $t = 3.1$, the wave portrait consists of lead shock L_2 followed in order by the contact C_1 , shock A_1 and shock B_2 . We observe that shock B_2 is traveling leftward, while the other two shocks are propagating to the right. Between L_2 and the contact surface the region is one of partial reaction, while the reaction is complete behind the contact. By $t = 3.3$ shock A_1 has overtaken the contact. The collision preserves the shock and the contact but generates a weak rarefaction traveling backward. The region between the contact and the shock A_1 is now an expanding site of enhanced reaction, as can be seen in the profiles of λ at times 3.3 and 3.5. Also, the shock B_2 is now traveling rightward, after having reflected off the piston face between times $t = 3.1$ and $t = 3.3$. The profiles in Fig. 22b, drawn for times $t = 4.0$ to $t = 4.8$, show that the shock A_1 continues to travel through the partially reacted material processed by the lead shock L_2 , strengthening the reaction as it does so. By $t = 4.4$ a thin region behind shock A_1 has appeared in which full consumption has occurred. At $t = 4.6$, this region has broadened as the shock A_1 has

Fig. 18 The formation of the initial reaction wave for Case 2. Profiles of volume fraction, density, reaction progress, pressure and temperature at $t = 0.1, 0.4, 0.6, 0.8,$ and 1.0 . The arrow indicates passage of time

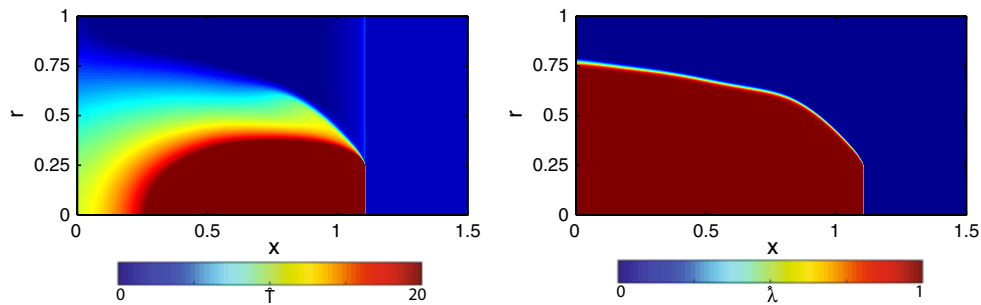
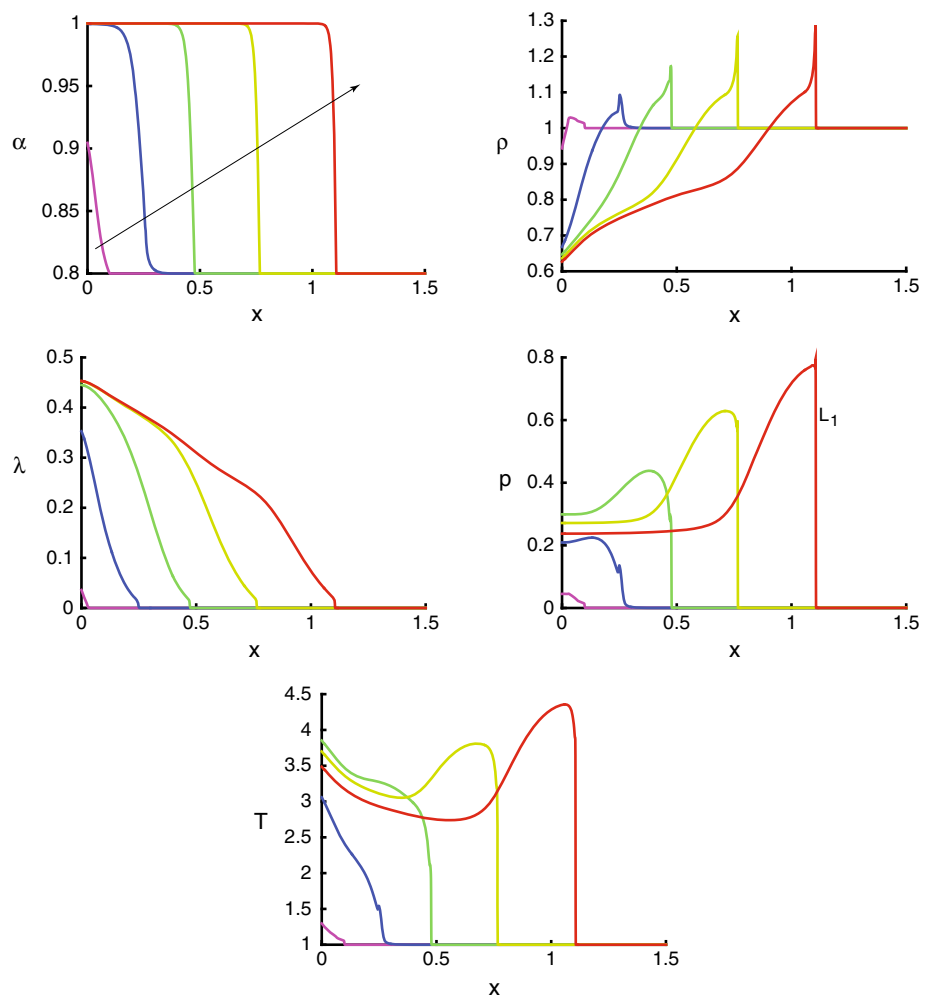


Fig. 19 Contour plots of the grain-scale variables \hat{T} (left) and $\hat{\lambda}$ (right) for Case 2 at $t = 1$

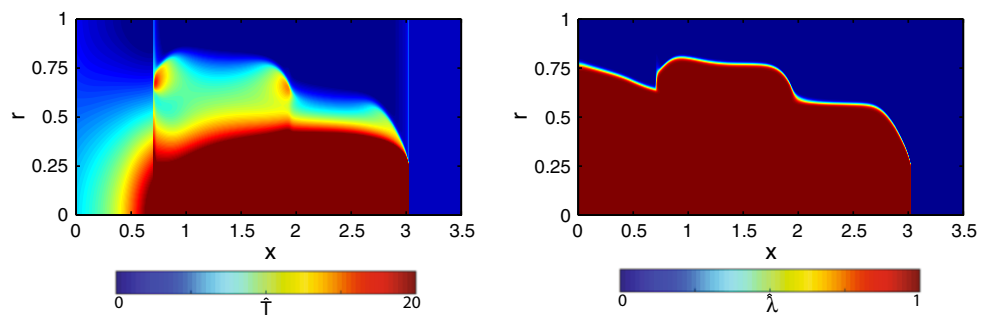
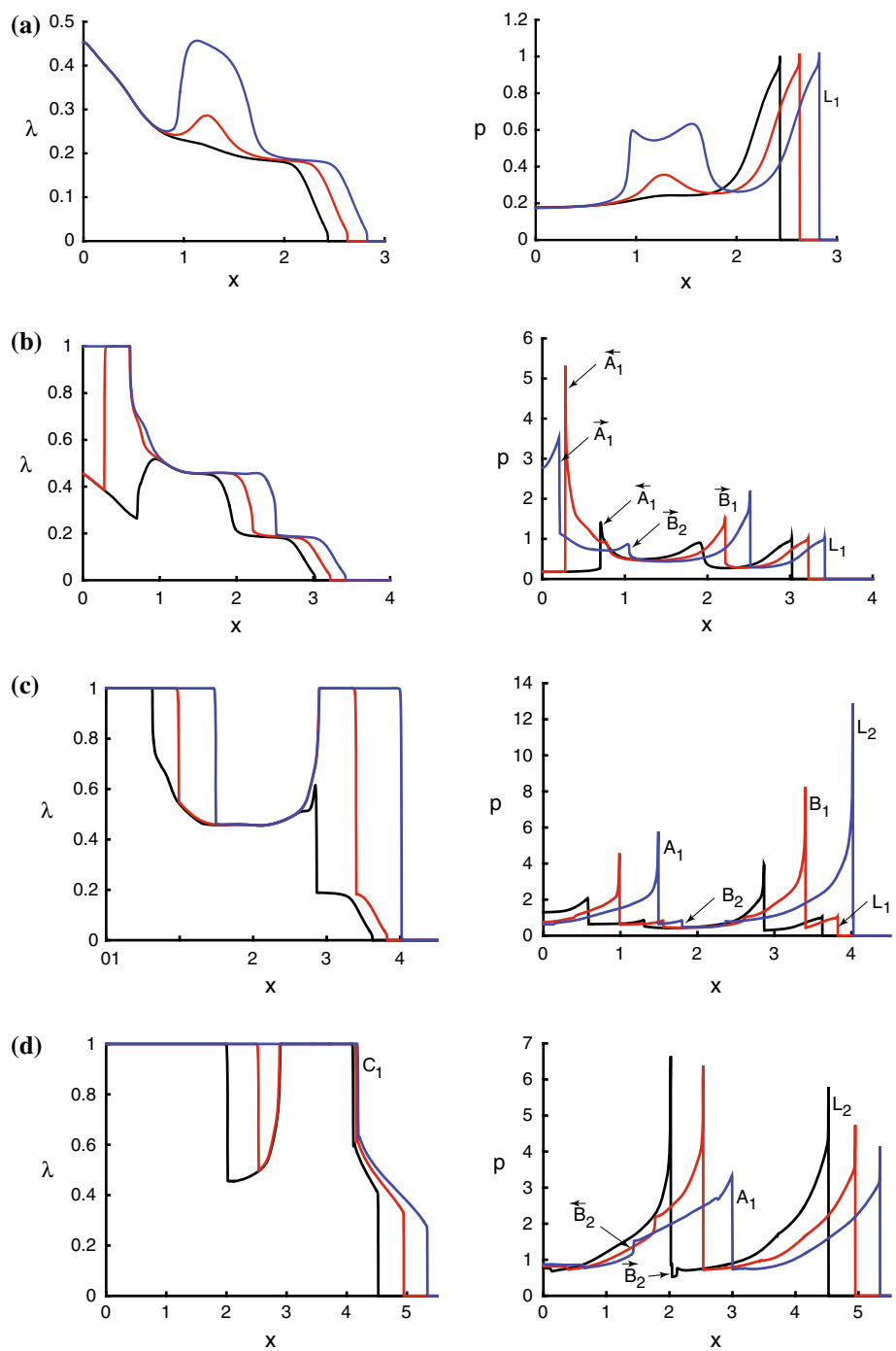


Fig. 20 Contour plots of the grain-scale variables \hat{T} (left) and $\hat{\lambda}$ (right) for Case 2 at $t = 2$

Fig. 21 Evolution of the secondary reaction zone for Case 2. Profiles of reaction progress and pressure
a at $t = 1.7, 1.8,$ and 1.9 ;
b at $t = 2.0, 2.1,$ and 2.2 ;
c at $t = 2.3, 2.4,$ and 2.5 ; and
d at $t = 2.6, 2.7,$ and 2.8

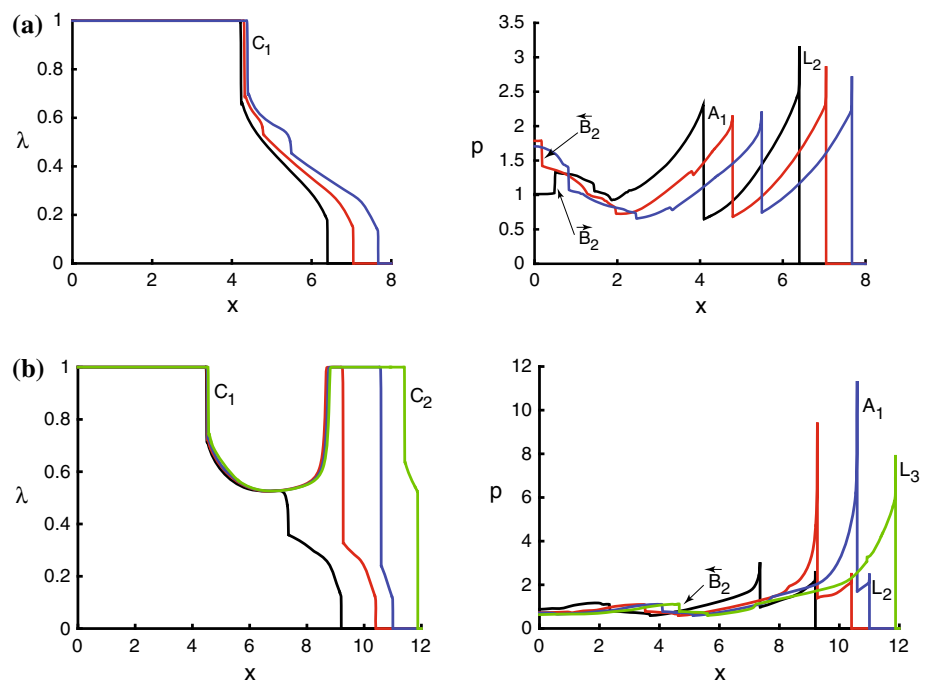


advanced further. Between this region and the contact the material is still only partially reacted. Shock A_1 is moving faster than the lead shock and by $t = 4.8$ has overtaken L_2 so that the transmitted shock becomes the new lead shock, L_3 . Also generated by the collision is a weak reflected shock, and more importantly a second contact, C_2 , separating partially reacted material ahead of it from fully reacted material behind.

6.2.4 Formation and propagation of the secondary reaction wave: Case 2, Cycle 3

Cycle 2 above ended with the appearance of a new lead shock, L_3 , followed by two contacts, C_2 and C_1 , each with an incomplete reaction zone ahead of it and a complete reaction zone behind it. The next stage of evolution is illustrated in the bulk-scale reaction-progress and pressure profiles collected

Fig. 22 Evolution of the secondary reaction zone, Cycle 2, for Case 2. Profiles of reaction progress and pressure **a** at $t = 3.1, 3.3,$ and 3.5 ; and **b** at $t = 4.0, 4.4, 4.6,$ and 4.8



in Fig. 23, covering the time span $t = 4.8$ to $t = 8.0$. The profiles of Fig. 23a show that between $t = 4.8$ and $t = 5.0$, the shock B_2 has crossed the contact C_1 . The result is a strengthening of the shock B_2 and an enhanced reaction between shock B_2 and the contact C_1 . By $t = 5.2$ a thin zone of complete reaction appears behind the shock B_2 . This situation is similar to what was seen in Cycle 2, Fig. 22a, around $t = 3.3$. Meanwhile, the lead shock L_3 continues to advance into the ambient region, with decreasing strength and a broadening zone of partial reaction behind it. The profiles of Fig. 23b show that by $t = 5.5$ the shock B_2 has grown considerably in strength and has nearly reached the right extremity of the partial reaction region, which is fully devoured by $t = 6.0$. At $t = 6.0$ and 6.5 , the shock B_2 finds itself in a fully reacted region, losing strength in the absence of any energy input from reaction. At $t = 7.0$, the shock B_2 has crossed the contact C_2 and entered a region of partial reaction, where it experiences a boost in strength as it enhances the reaction. The profiles of Fig. 23c show that reaction enhancement and shock strengthening continue at times $t = 7.4$ to $t = 8.0$, and that the buildup of reaction behind the shock B_2 gives rise to a reaction wave propagating backward into the partially reacted material. The lead shock L_3 continues to advance at an essentially steady rate. The final stage of Cycle 3 is displayed in the profiles of Fig. 24, plotted from $t = 10.0$ to 10.8 . These profiles show the secondary shock B_2 continuing to strengthen as it closes in on the lead shock L_3 . The two shocks collide between $t = 10.6$ and $t = 10.8$, giving birth to a new lead shock, L_4 , and a new contact C_3 . The shock L_4 exhibits a drop in strength as it propagates into the ambient material.

To summarize, the lower crossover temperature makes the explosive more reactive but the repetitive character of evolution, wherein a typical cycle consists of a secondary shock overtaking the lead shock and generating a new contact where reaction enhancement and the birth of a new secondary shock will occur in due course, is preserved.

6.3 Case 3: Lower diffusion parameter

We now consider the case for which the value of the diffusion parameter k has been reduced from 0.03 for the base case to 0.02. Diminution in the diffusive transport of heat leads to competing effects at the grain scale. On the one hand, energy is lost at a reduced rate from the deposition region within the grains so that temperature there is higher, thereby increasing the reaction rate and hence the initial rate of flame spread. On the other hand, diffusive preheating of the ambient material ahead of the flame occurs at a reduced rate, thereby lowering the flame speed. The outcome of this competition is a scenario that is altered in fine details from the two cases already considered, but is preserving of the overall, cyclical nature of the evolutionary process. A brief description emphasizing the differences follows.

6.3.1 Formation and propagation of the initial reaction wave, Case 3

The early-time behavior following piston impact is essentially the same as that for the base case. The profiles of the

Fig. 23 Evolution of the secondary reaction zone, Cycle 3, for Case 2. Profiles of reaction progress and pressure **a** at $t = 4.8, 5.0,$ and 5.2 ; **b** at $t = 5.5, 6.0, 6.5,$ and 7.0 ; and **c** at $t = 7.4, 7.6, 7.8,$ and 8.0

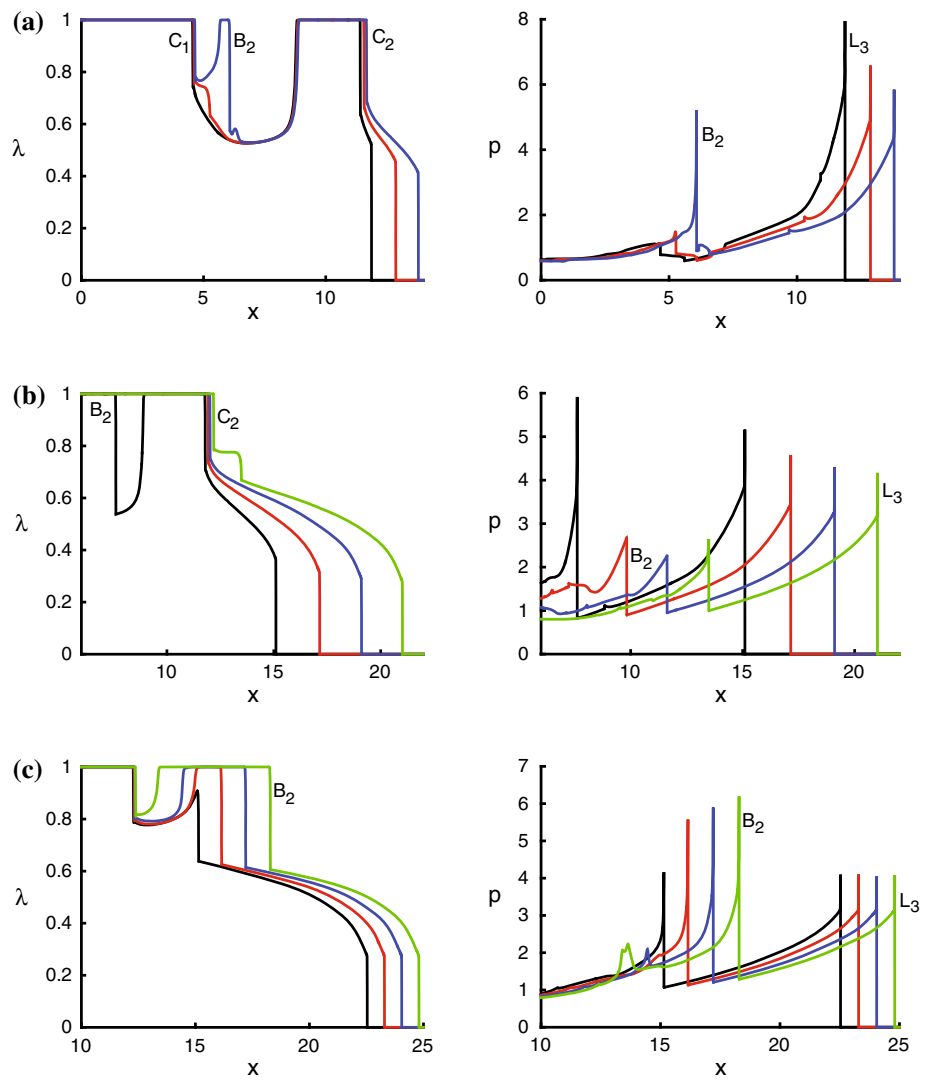
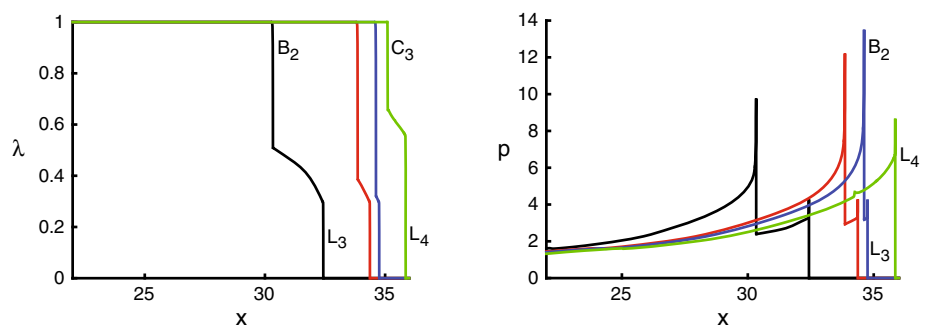


Fig. 24 Evolution of the secondary reaction zone, Cycle 3, for Case 2. Profiles of reaction progress and pressure at $t = 10.0, 10.5, 10.6,$ and 10.8



bulk properties, not shown for the case under consideration in the interest of brevity, are nearly identical to those for the base case displayed in Fig. 5, with the exception that temperature and reaction progress near the piston face are now slightly higher.

6.3.2 Formation and propagation of the secondary reaction wave: Case 3, Cycle 1

As in the previous cases the lead wave steepens into a shock, L_1 , and continues its advance. Unlike Case 1 where a sin-

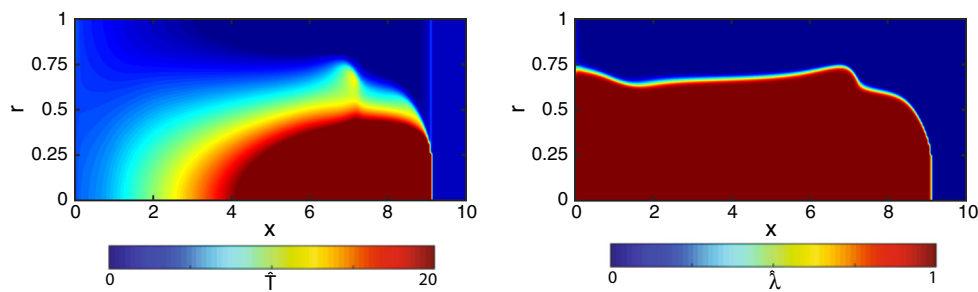


Fig. 25 Contour plots of the grain-scale variables $\hat{\lambda}$ and \hat{T} , at $t = 6.0$ for Case 3

gle secondary reaction zone developed at the piston (Fig. 9), or Case 2 where a broad secondary reaction zone appeared between the piston face and the lead shock (Fig. 20), two separate zones of secondary reaction now emerge. These will be referred to as the trailing and leading zones, where the trailing zone is situated at the piston as before and the leading zone sits between the piston and the lead shock. These zones are visible in the contour plots of grain-scale reaction progress and temperature at $t = 6.0$, shown in Fig. 25. The trailing zone has the same grain-scale origin as that in Case 1; a flame propagating radially outward stalls before reaching the grain boundary, and the pocket of unreacted explosive ahead of it is ignited by heat transfer from the burned to the unburned side. The process is illustrated in Fig. 26, which displays the profiles of grain-scale temperature and reaction progress against r at the piston face. A comparison with the corresponding profiles for Case 1 drawn in Fig. 7 shows that the process is somewhat faster in the present case. Specifically, the reverse flame near the boundary $r = 1$ now develops around $t = 6.3$, Fig. 26d, rather than around $t = 6.7$ for Case 1. The origin of the leading secondary reaction zone, between the piston and the lead shock, is analogous to that seen in Case 2.

The corresponding development at the bulk scale is shown in the profiles of reaction progress and pressure, displayed in Fig. 27a from $t = 1.0$ to $t = 6.0$. Evolution of enhanced reactivity at the two secondary zones identified above is evident in these profiles. Local bumps in pressure in the two zones appear prominently at $t = 6.0$.

The profiles in Fig. 27b, plotted from $t = 6.4$ to $t = 6.8$, show further strengthening of both secondary reaction zones and the development of a shock in each, reminiscent of similar developments in Case 2 that are displayed in Fig. 21. At $t = 6.8$, the trailing-zone shock A_1 is stronger than the leading-zone shock B_1 , strong enough so that the reaction is complete behind the shock A_1 but only partially complete behind the shock B_1 . The profiles in Fig. 27c, plotted from $t = 7.0$ to $t = 7.4$, show that at $t = 7.0$ shock A_1 has moved closer to shock B_1 , which in turn is about to collide with the lead shock L_1 . The collision occurs just before $t = 7.2$ and results, as in previous cases, in a transmitted

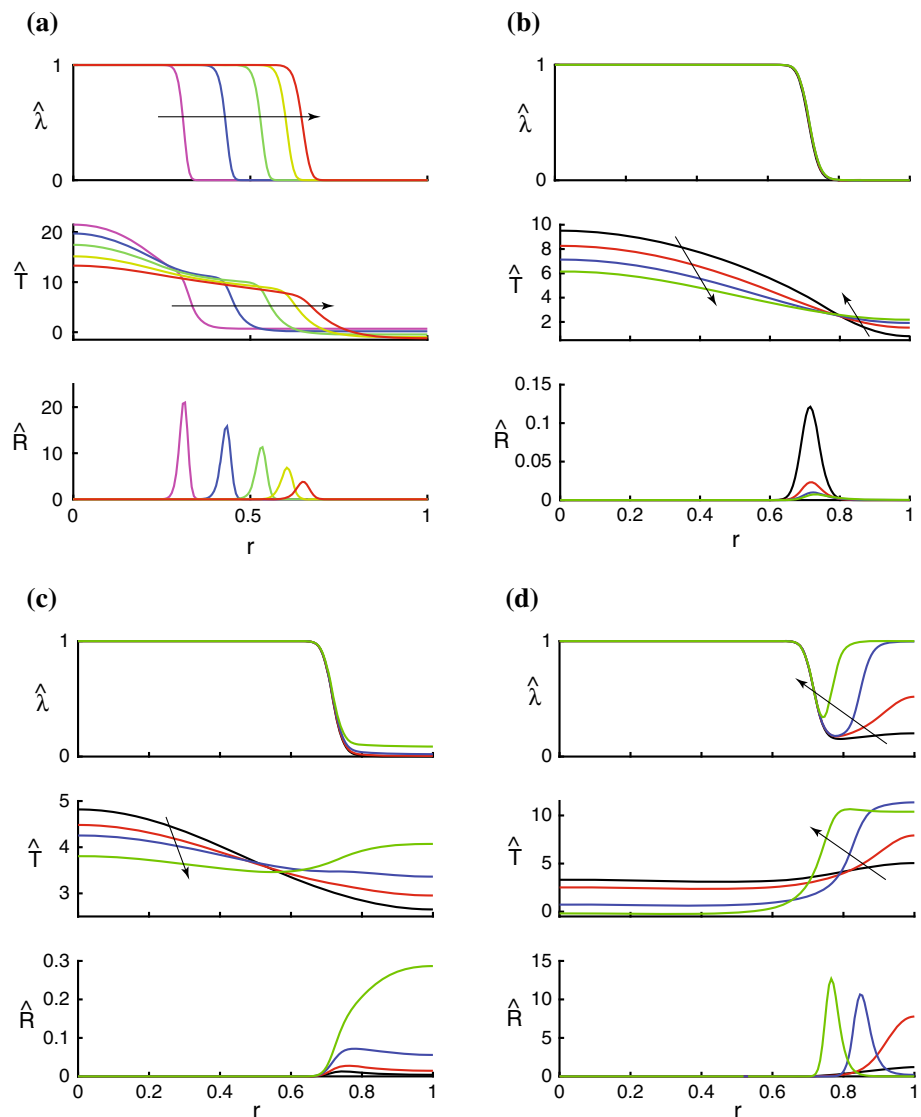
shock L_2 , a contact C_1 and a weak reflected shock T_2 . At its birth, the shock L_2 is strong enough to produce a thin zone of complete reaction behind it, but as the profiles at $t = 7.4$ show, L_2 loses strength quickly as it travels through the ambient material, leaving a zone of only partial reaction between it and the contact C_1 , while the aforementioned thin zone of complete reaction persists behind the contact C_1 . At this time, the reflected shock T_2 is stronger, and shock A_1 continues to advance and fully consume the partially reacted material through which it travels, even as it loses strength somewhat due to the positive gradient in λ ahead of it.

6.3.3 Formation and propagation of the secondary reaction wave: Case 3, Cycle 2

Figure 28a shows the bulk-scale reaction progress and pressure profiles from $t = 8.3$ to $t = 8.9$. By $t = 8.3$ the wave structure just described, consisting of lead shock L_2 , contact C_1 , trailing shock A_1 and reflected shock T_2 as its main ingredients, has undergone a slight adjustment in that shock T_2 has passed through shock A_1 and is now receding away from it. At $t = 8.7$, shock A_1 , continuing to weaken yet still causing full consumption of the material through which it passes, is approaching the thin zone of full reaction behind the contact C_1 . At $t = 8.9$, shock A_1 has advanced through most of this zone, and the resulting loss of reactive support has weakened the shock still further, now rather dramatically. The loss of pressure at the shock has created a rarefaction R_1 in the pressure profile behind the shock. The reflected shock T_2 has also lost strength upon passage through fully reacted material. There are other small-scale disturbances in the pressure profile in the fully reacted region, some traveling to the right and others to the left.

Bulk-scale reaction progress and pressure profiles from $t = 9.1$ to $t = 9.7$ are displayed in Fig. 28b. At $t = 9.1$, shock A_1 has just crossed contact C_1 into the region of partial reaction behind shock L_2 . Noteworthy features are the strengthening of the shock due to the reinstatement of reaction and a second rarefaction R_2 behind the shock. The

Fig. 26 Flame quenching and rebirth at the piston face for Case 3. Profiles of $\hat{\lambda}$, \hat{T} , and grain-scale reaction rate at **a** $t = 0.2, 0.4, 0.6, 0.8,$ and 1.0 ; **b** $t = 2.0, 2.5, 3.0,$ and 3.5 ; **c** $t = 4.5, 5.0, 5.5,$ and 6.0 ; and **d** $t = 6.2, 6.3, 6.4,$ and 6.5 . Arrows indicate progression of time



reason for this additional pressure loss is the presence of a weak temperature dip ahead of the contact C_1 , which is not shown in the figure. As shock A_1 advances into the partially reacted medium, it continues to get stronger, and as the profiles at $t = 9.5$ and $t = 9.7$ show, material passing through this shock experiences an increasing amount of reactant consumption. In fact, at $t = 9.7$ the reaction immediately behind the shock is complete. Meanwhile, the lead shock has settled down to a steady profile.

The profiles in Fig. 28c, drawn for times $t = 10.0$ to $t = 11.1$, show shock A_1 to be gathering strength still further and gaining over the lead shock L_2 , as it leaves in its wake an expanding region of complete reaction. Only a narrowing pocket of partial reaction survives ahead of contact C_1 . At $t = 10.9$, shocks A_1 and L_2 are about to collide, and the post-collision profiles at $t = 11.1$ show a new lead shock L_3 and a new contact C_2 , along with the hint of a weak reflected

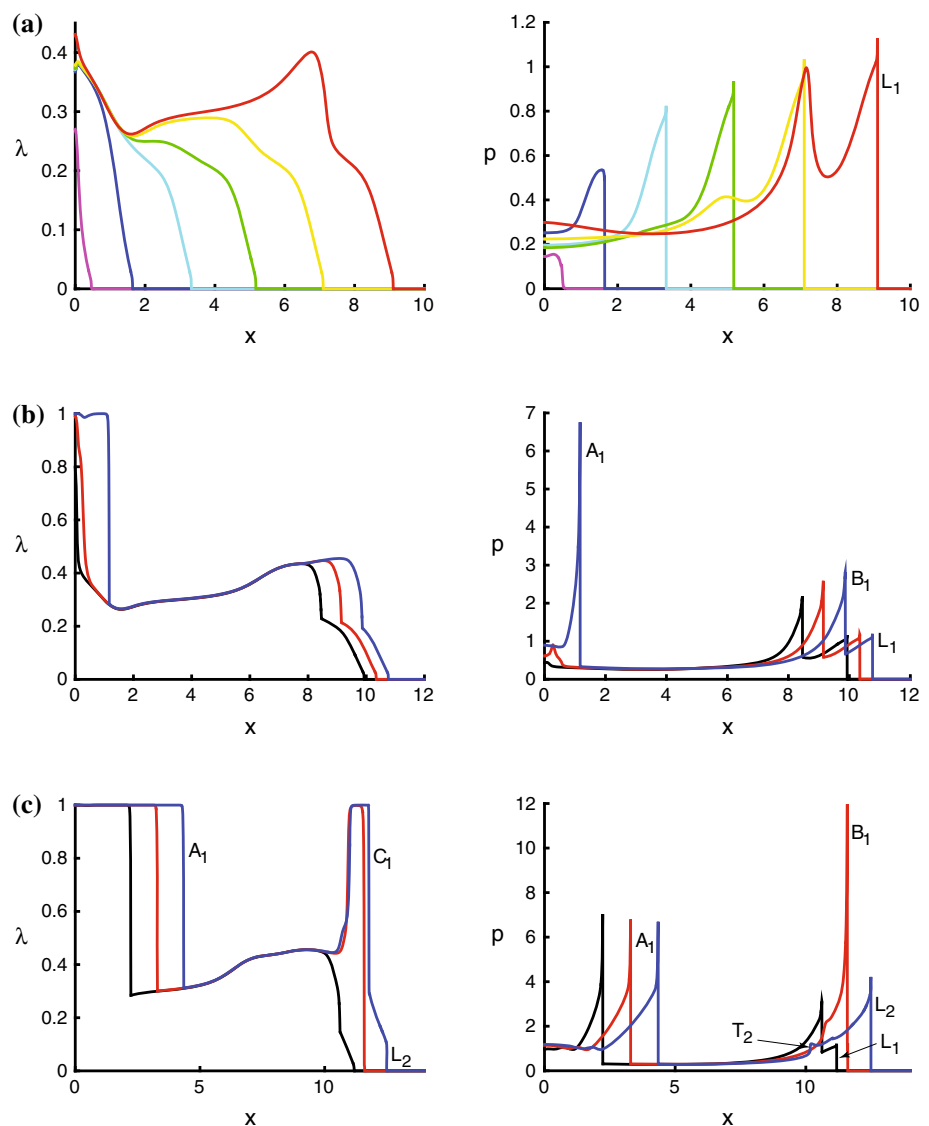
shock. This structure is reminiscent of that in Cycle 2 of Case 2, discussed earlier in Sect. 6.2.3.

6.3.4 Formation and propagation of the secondary reaction wave: Case 3, Cycle 3

Figure 29a displays the profiles of reaction progress and pressure from $t = 13.0$ to $t = 16.0$. For clarity we have elected to limit the display to the region in the vicinity of the wave-head. The profiles show the lead shock L_3 followed by the contact C_2 which separates the fully reacted region behind it from the partially reacted region in front of it. Behind the contact but closing in on it is a weak shock D , the forward-most remnant of the pressure disturbances identified in the pressure profile at $t = 8.9$ in Fig. 28a.

The profiles in Fig. 29b, drawn for times from $t = 16.1$ to $t = 16.7$, show the shock D overtaking the contact C_2 at

Fig. 27 Evolution of the secondary reaction zones, Cycle 1, for Case 3. Profiles of reaction progress and pressure **a** at $t = 1.0, 2.0, 3.0, 4.0, 5.0,$ and 6.0 ; **b** at $t = 6.4, 6.6,$ and 6.8 ; and **c** at $t = 7.0, 7.2,$ and 7.4



$t = 16.1$. The shock is strengthened by chemical reaction upon entering the partially reacted region and by $t = 16.7$ has become stronger than the lead shock, causing complete consumption of the material passing through it. Profiles for times $t = 20.0$ to $t = 23.0$, shown in Fig. 29c, confirm the inevitable: Shock D advances toward the lead shock and collides with it at $t = 22.2$, generating a new lead shock L_4 and a contact C_3 . Thus, the scenario is similar to those for Cases 1 and 2.

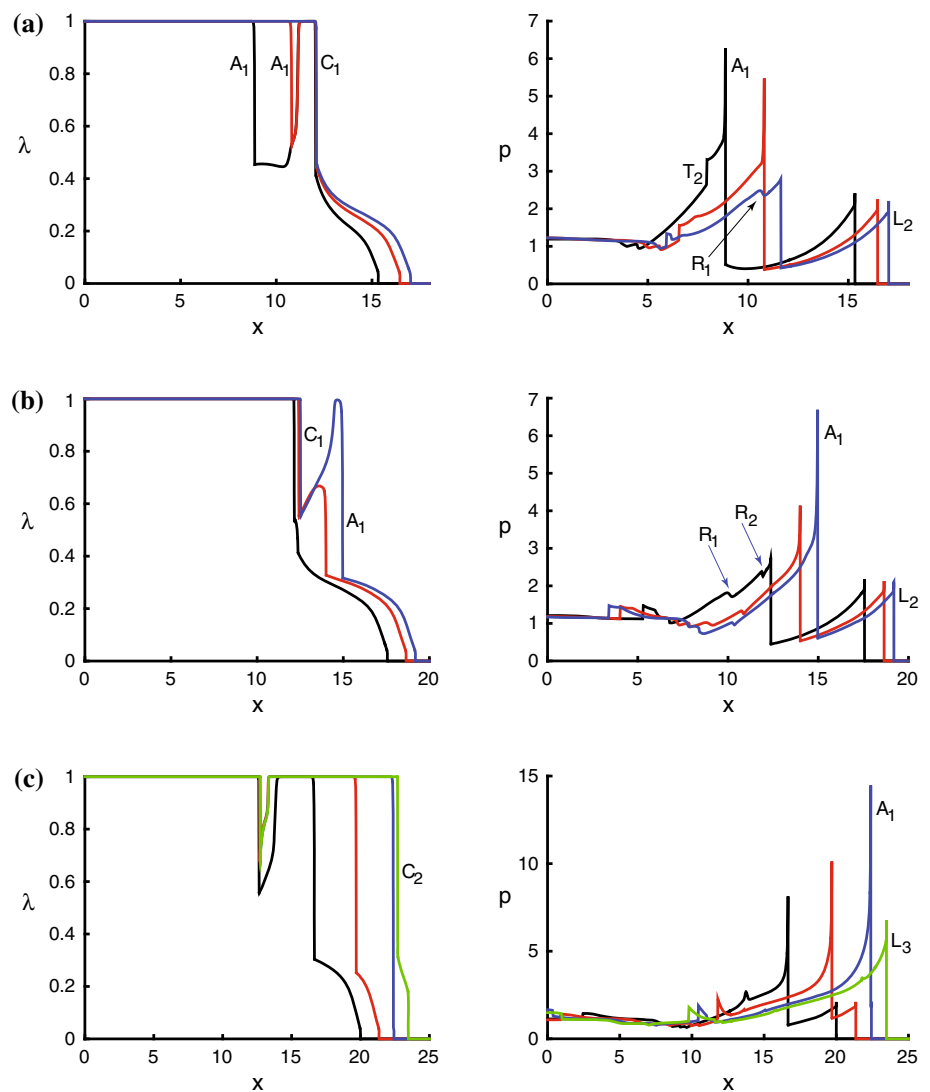
7 Conclusions

A comprehensive computational study of compaction-induced detonation in a high-energy granular explosive has been conducted. The explosive is treated as a porous solid, modeled

at the bulk scale as a compacting continuum and at the meso-scale as a collection of identical, closely packed spherical grains capable of undergoing reaction and conductive heat transport. The two scales are coupled in an energetically consistent manner. Impact by the driving piston compacts the bulk and induces plastic deformation and localized energy deposition in the grains at the sites of intergranular contact. The resulting temperature rise creates hot spots where reaction begins preferentially. The space-averaged reaction progress at the grain scale determines the reaction progress at the bulk scale. Thus, the grain-scale model may be viewed as the vehicle that supplies an averaged reaction rate to the bulk scale.

Earlier work by Gonthier had focused on steady traveling waves, with an eye on assessing whether the hot-spot temperatures were high enough to result in the onset of sus-

Fig. 28 Evolution of the secondary reaction zones, Cycle 2, for Case 3. Profiles of reaction progress and pressure **a** at $t = 8.3, 8.7,$ and 8.9 ; **b** at $t = 9.1, 9.5,$ and 9.7 ; and **c** at $t = 10.0, 10.5, 10.9,$ and 11.1

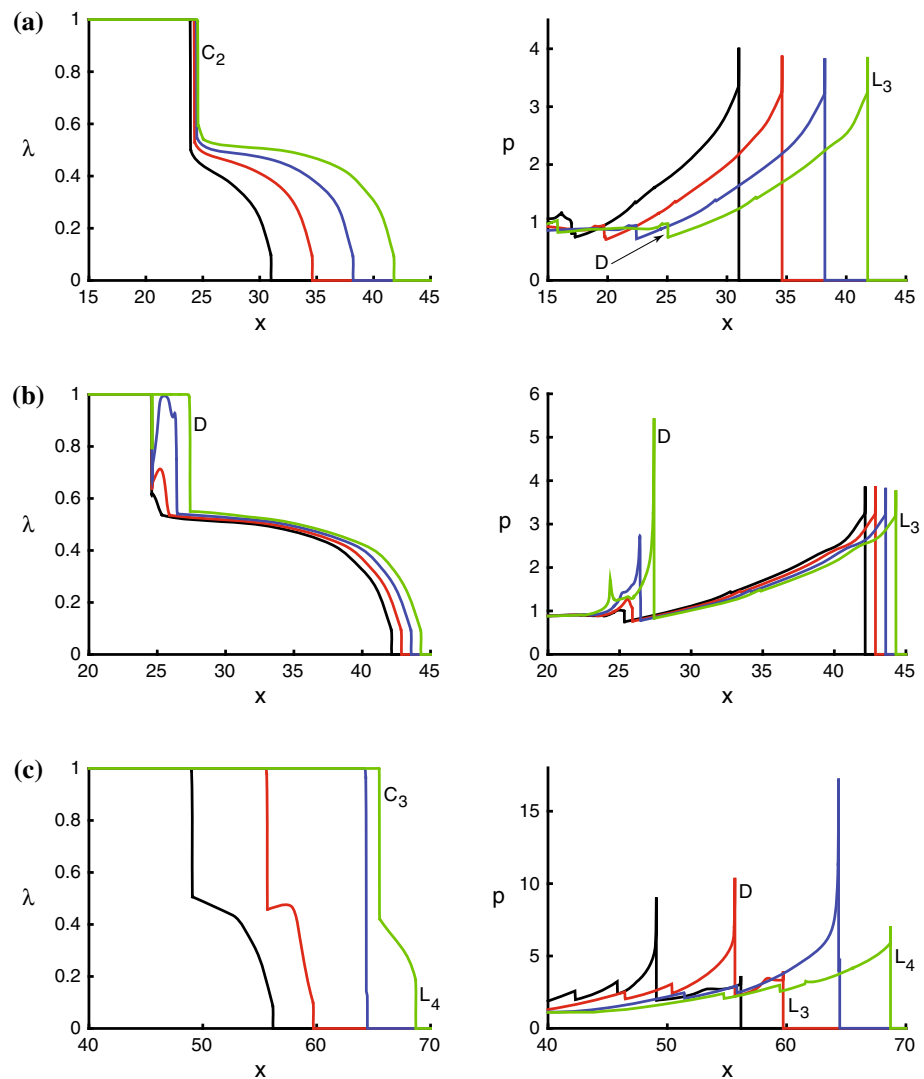


tained combustion. We have examined the transient behavior in detail, for idealized modeling choices to be sure, to discover the evolutionary processes exhibited by the model and the eventual outcome resulting therefrom. The study has been conducted for three representative parameter choices and finds that none of the cases exhibits a steady traveling wave; rather, combustion proceeds in a cyclical fashion in each case. Typically, a primary lead shock induced by compaction and supported by reaction loses strength as it propagates through ambient material. Reaction in the partially reacted material behind the primary shock generates a stronger and faster secondary shock which overtakes the primary shock to become the new lead shock, and the process repeats itself. Although the precise mechanisms responsible for the creation of the secondary shock are dependent upon the prevailing parameters, the general features are preserved from one case to the next. It is worth pointing out that we are

not aware of experimental evidence that would support the above outcome.

The evolutionary conduct of the model depends, of course, upon the modeling choices made. For computational feasibility we have chosen a larger diffusion coefficient and a weaker temperature sensitivity of the reaction rate than realism would require. Some experimentation with changing the relevant parameters shows little qualitative change in the results. Other choices include the neglect of the interstitial gas and the treatment of the explosive as a single-phase material, the adoption of a simple equation of state, the localization and energy-deposition strategies, the assumption of incompressibility at the grain scale and the absence of diffusive communication among grains. Accounting for the gaseous constituents, both ambient gas and reaction products, would require the more complex multiphase approach. Adoption of a realistic equation of state would also add to

Fig. 29 Evolution of the secondary reaction zone, Cycle 3, for Case 3. Profiles of reaction progress and pressure **a** at $t = 13.0, 14.0, 15.0,$ and 16.0 ; **b** at $t = 16.1, 16.3, 16.5,$ and 16.7 ; and **c** at $t = 20.0, 21.0, 22.2,$ and 23.0



the complexity of the model. In recent work [27] with the two-phase model and with realistic equations of state we have shown that certain aspects of the results can be quite sensitive to the reaction rate and the equations of state. Further work exploring relaxation of some of the assumptions is planned.

Acknowledgements Research support was provided by Los Alamos National Laboratory under Contract 336767. The work of JRG was performed under the auspices of the US Department of Energy (DOE) by LLNL under Contract DE-AC52-07NA27344. LLNL Report LLNL-JRNL-735470.

References

- Gonthier, K.A.: Modeling and analysis of reactive compaction for granular energetic solids. *Combust. Sci. Technol.* **175**(9), 1679–1709 (2003). doi:[10.1080/00102200302373](https://doi.org/10.1080/00102200302373)
- Lee, E.L., Tarver, C.M.: Phenomenological model of shock initiation in heterogeneous explosives. *Phys. Fluids* **23**(12), 2362–2372 (1980). doi:[10.1063/1.862940](https://doi.org/10.1063/1.862940)
- Tarver, C.M., McGuire, E.M.: Reactive flow modeling of the interaction of TATB detonation waves with inert materials. In: *The Twelfth Symposium (International) on Detonation*, pp. 641–649 (2002)
- Tarver, C.M.: Ignition and growth modeling of LX-17 hockey puck experiments. *Propellants Explos Pyrotech.* **30**, 109–117 (2005). doi:[10.1002/prop.200400092](https://doi.org/10.1002/prop.200400092)
- Baer, M.R., Nunziato, J.W.: A two-phase mixture theory for the deflagration-to-detonation transition (DDT) in reactive granular materials. *Int. J. Multiph. Flow* **12**, 861–889 (1986). doi:[10.1016/0301-9322\(86\)90033-9](https://doi.org/10.1016/0301-9322(86)90033-9)
- Butler, P.B., Krier, H.: Analysis of deflagration to detonation transition in high-energy solid propellants. *Combust. Flame* **63**(1–2), 31–48 (1986). doi:[10.1016/0010-2180\(86\)90109-4](https://doi.org/10.1016/0010-2180(86)90109-4)
- Powers, J.M., Stewart, D.S., Krier, H.: Theory of two-phase detonation, part I: modeling. *Combust. Flame* **80**(3–4), 264–279 (1990). doi:[10.1016/0010-2180\(90\)90104-Y](https://doi.org/10.1016/0010-2180(90)90104-Y)
- Powers, J.M., Stewart, D.S., Krier, H.: Theory of two-phase detonation, part II: structure. *Combust. Flame* **80**(3–4), 280–303 (1990). doi:[10.1016/0010-2180\(90\)90105-Z](https://doi.org/10.1016/0010-2180(90)90105-Z)

9. Gonthier, K.A., Powers, J.M.: A numerical investigation of transient detonation in granulated material. *Shock Waves* **6**, 183–195 (1996). doi:[10.1007/BF02511375](https://doi.org/10.1007/BF02511375)
10. Bdzil, J.B., Menikoff, R., Son, S.F., Kapila, A.K., Stewart, D.S.: Two-phase modeling of deflagration-to-detonation transition in granular materials: a critical examination of modeling issues. *Phys. Fluids* **11**(2), 378–402 (1999). doi:[10.1063/1.869887](https://doi.org/10.1063/1.869887)
11. Gonthier, K.A., Powers, J.M.: A high-resolution numerical method for a two-phase model of deflagration-to-detonation transition. *J. Comput. Phys.* **163**, 376–433 (2000). doi:[10.1006/jcph.2000.6569](https://doi.org/10.1006/jcph.2000.6569)
12. Saurel, R., Abgrall, R.: A simple method for compressible multi-fluid flows. *SIAM J. Sci. Comput.* **21**(3), 1115–1145 (1999). doi:[10.1137/S1064827597323749](https://doi.org/10.1137/S1064827597323749)
13. Saurel, R., Lemetayer, O.: A multiphase model for compressible flows with interfaces, shocks, detonation waves and cavitation. *J. Fluid Mech.* **431**, 239–271 (2001). doi:[10.1017/S002211200003098](https://doi.org/10.1017/S002211200003098)
14. Schwendeman, D.W., Wahle, C.W., Kapila, A.K.: The Riemann problem and a high-resolution Godunov method for a model of compressible two-phase flow. *J. Comput. Phys.* **212**, 490–526 (2006). doi:[10.1016/j.jcp.2005.07.012](https://doi.org/10.1016/j.jcp.2005.07.012)
15. Schwendeman, D.W., Wahle, C.W., Kapila, A.K.: A study of detonation evolution and structure for a model of compressible two-phase reactive flow. *Combust. Theory Model.* **12**, 159–204 (2008). doi:[10.1080/13647830701564538](https://doi.org/10.1080/13647830701564538)
16. Michael, L., Nikiforakis, N.: A hybrid formulation for the numerical simulation of condensed phase explosives. *J. Comput. Phys.* **316**, 193–217 (2016). doi:[10.1016/j.jcp.2016.04.017](https://doi.org/10.1016/j.jcp.2016.04.017)
17. Baer, M.R.: Mesoscale Modeling of Shocks in Heterogeneous Reactive Materials. In: *Shock Wave Science and Technology Reference Library*, pp. 321–356. Springer, Berlin (2007). doi:[10.1007/978-3-540-68408-4_8](https://doi.org/10.1007/978-3-540-68408-4_8)
18. Zhang, J., Jackson, T.L., Buckmaster, J., Freund, J.B.: Numerical modeling of shock-to-detonation transition in energetic materials. *Combust. Flame* **159**, 1769–1778 (2012). doi:[10.1016/j.combustflame.2011.11.010](https://doi.org/10.1016/j.combustflame.2011.11.010)
19. Jackson, T.L., Buckmaster, J.D., Zhang, J., Anderson, J.: Pore collapse in an energetic material from the micro-scale to the macro-scale. *Combust. Theory Model.* **19**, 347–381 (2015). doi:[10.1080/13647830.2015.1026401](https://doi.org/10.1080/13647830.2015.1026401)
20. Zhang, J., Jackson, T.L.: Direct detonation initiation with thermal deposition due to pore collapse in energetic materials—towards the coupling between micro- and macro scales. *Combust. Theory Model.* **21**, 248–273 (2017). doi:[10.1080/13647830.2016.1218053](https://doi.org/10.1080/13647830.2016.1218053)
21. Menikoff, R.: Deflagration wave profiles. Tech. Rep. LA-UR-12-20353, Los Alamos National Laboratory (2012)
22. Ozlem, M., Schwendeman, D.W., Kapila, A.K., Henshaw, W.D.: A numerical study of shock-induced cavity collapse. *Shock Waves* **22**, 89–117 (2012). doi:[10.1007/s00193-011-0352-9](https://doi.org/10.1007/s00193-011-0352-9)
23. Henshaw, W.D., Schwendeman, D.W.: An adaptive numerical scheme for high-speed reactive flow on overlapping grids. *J. Comput. Phys.* **191**(2), 420–447 (2003). doi:[10.1016/S0021-9991\(03\)00323-1](https://doi.org/10.1016/S0021-9991(03)00323-1)
24. Banks, J.B., Schwendeman, D.W., Kapila, A.K., Henshaw, W.D.: A high-resolution Godunov method for multi-material flows on overlapping grids. *J. Comput. Phys.* **223**, 262–297 (2007). doi:[10.1016/j.jcp.2006.09.014](https://doi.org/10.1016/j.jcp.2006.09.014)
25. Henshaw, W.D., Schwendeman, D.W.: Parallel computation of three-dimensional flows using overlapping grids with adaptive mesh refinement. *J. Comput. Phys.* **227**, 7469–7502 (2008). doi:[10.1016/j.jcp.2008.04.033](https://doi.org/10.1016/j.jcp.2008.04.033)
26. Schwendeman, D.W., Kapila, A.K., Henshaw, W.D.: A study of detonation diffraction and failure for a model of compressible two-phase reactive flow. *Combust. Theory Model.* **14**, 331–366 (2010). doi:[10.1080/13647830.2010.489955](https://doi.org/10.1080/13647830.2010.489955)
27. Gambino, J., Kapila, A.K., Schwendeman, D.W.: Sensitivity of run-to-detonation distance in practical explosives. *Combust. Theory Model.* **20**, 1088–1117 (2016). doi:[10.1080/13647830.2016.1253872](https://doi.org/10.1080/13647830.2016.1253872)